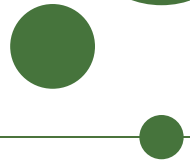


UNIVERSITY OF COPENHAGEN
FACULTY OF SCIENCE



PhD thesis

Michael. J. Larson

A Search for Tau Neutrino Appearance with IceCube-DeepCore

Advisor: Dr. D. Jason Koskinen

Handed in: March 8, 2018

Contents

1	Introduction	9
1.1	The History of the Neutrino	9
1.2	History of Cosmic Rays	10
1.3	Atmospheric Neutrinos	11
1.4	The Standard Model	12
1.5	Methods of Detection	16
2	Neutrino Oscillations	20
2.1	Oscillation Theory and the PMNS Matrix	20
2.2	Experimental Constraints on Neutrino Oscillations	23
2.3	Solar Neutrinos: A Hint of Multiple Flavors	23
2.4	Super-Kamiokande and Atmospheric Neutrinos	25
2.5	Unitarity and Sterile Neutrinos	26
3	The IceCube Detector	32
3.1	The DOM: The Basic Unit of IceCube	32
3.2	The Geometry of the Detector	35
3.3	Optical Properties of the Antarctic Glacier	39
4	Simulation of the IceCube-DeepCore Detector	42
4.1	Monte Carlo Generators	42
4.2	Propagation of the Particles and Light	46
4.3	Simulating the Detector Electronics	48
5	Updates to the Noise Simulation	50
5.1	A Summary of Previous Fits	50
5.2	Limitations and Disagreement with Previous Fits	50
5.3	Low-dt Noise from Vuvuzela	51
5.4	Updating the Fitting Code	52
5.5	Results of New Noise Fits	53
6	Low-Energy Muon Simulation	55
6.1	Long-Frame CORSIKA for DeepCore	55
6.2	MuonGun for DeepCore	56
6.3	Simulation Efficiency with KDE Filtering	56
7	GRECO: An Event Selection at the Limits of DeepCore	58
7.1	Low-En Level 3 Cuts	58
7.2	The Properties of the GRECO Event Selection	73
8	A Search for Tau Neutrinos from Oscillations	76

8.1	Expectations from Monte Carlo	76
8.2	Parametrizing the Tau Neutrino Appearance	77
8.3	Systematics Considerations	79
8.4	The Method of Maximum Likelihood	85
8.5	Expected Sensitivity to Appearance	89
8.6	Fitting Data	95
8.7	Results from the Search for Appearance	102
8.8	Complementary Measurements from This Analysis	107
8.9	New Constraints on Detector Systematics	108

List of Figures

1.1	The number of active neutrinos as measured by ALEPH, DELPHI, L3, and OPAL. The data from the four experiments strongly favors only three neutrinos coupling to the Z boson. Image taken from [9].	10
1.2	The cosmic ray spectrum covers many orders of magnitude and has been verified by many experiments to high precision. The various features are thought to be caused by multiple sources at different scales. Image taken from [17]	12
1.3	The expected neutrino flux at Kamioka mine, Japan (Super-Kamiokande, top left), Ino Peak, India (India-based Neutrino Observatory, top right), the South Pole (IceCube, bottom left), and Pyhasalmi mine, Finland (EMMA experiment, bottom right) as a function of energy. Note that the neutrino and anti-neutrino fluxes are characterized separately. The differences in the flux at each site is due to differences in the Earth's magnetic field and temperature profile. Figure taken from [18].	13
1.4	The expected flux of 3.2 GeV neutrinos at Kamioka mine, Japan; Ino Peak, India; the South Pole; and Pyhasalmi mine, Finland as a function of zenith angle. A value of $\cos \theta_Z = -1$ indicates neutrinos passing through the entire Earth and entering the detector from below while a value of $\cos \theta_Z = +1$ indicates neutrinos interacting in the atmosphere directly above the detector. The differences in the flux at each site is due to differences in the Earth's magnetic field and temperature profile. Figure taken from [18].	13
1.5	The Standard Model of particle physics is made up of charged and uncharged leptons, quarks, and the various bosons. Image taken from [19]	14
1.6	Feynman diagrams showing the interaction vertex of the neutrino with the W and Z boson.	14
1.7	The relative contributions to the cross section for ν (left) and $\bar{\nu}$ (right). The QE events dominate below 1 GeV while the DIS events dominate above 10 GeV. Note the different scales for the neutrino and antineutrinos. Images taken from [20]	15

1.8	A Feynman diagram showing an example of a CC neutrino DIS interaction. An incident muon neutrino interacts with a quark inside of a proton. The result is a hadronic shower as well as a charged muon. Diagram taken from [formaggio-xsec]	16
1.9	An example of the energy loss ($\frac{-dE}{dx}$) calculated for muons incident on copper. Note the radiative losses due to bremsstrahlung, pair production, and photonuclear interactions above 1 TeV. Note also the labeled minimum demonstrating the energy of a minimum ionizing particle. Image taken from [17].	18
2.1	The first atmospheric neutrino oscillation measurements from the Super-K experiment. (a) The ν_e -like events show no shape in L/E, as expected from a lack of neutrino oscillations. The ν_μ -like interactions, however, show a clear drop, indicating the presence of oscillation effects. (b) Using the two neutrino approximation, Super-K produced contours of the best-fit oscillation parameters for $\nu_\mu \rightarrow \nu_\tau$ oscillations. Both figures from [56]	25
2.2	The global best-fit values for the three flavor neutrino oscillation fits as of November 2017. The first column shows results assuming the normal ordering while the second column shows the results for the inverted ordering. Image taken from [58]	26
2.3	Expectations (a) and results (b) of searches for sterile neutrinos in the neutral current interactions. (a) Effect of three hypothetical sterile neutrinos on the measurements of the MINOS detector [63]. "ND" and "FD" refer to the near and far detector of MINOS respectively. The sterile neutrinos have a small effect on the main oscillation minimum in the charged current channel, but up to 15% of the neutral current events are lost. (b) The results of the NO ν A search for sterile neutrinos using neutral current events. The limits are interpreted in terms of the 4x4 PMNS mixing elements in order to compare to searches with charged current interactions in Super-Kamiokande [65] and IceCube [66].	27
2.4	The results of the tests using 2.25 (solid) and 2.26 (dotted). A smaller value on the x-axis indicates a tighter constraint on observed unitarity of the 3x3 mixing matrix. Tests involving only muon or electron flavors show significantly tighter constraints than those including the tau flavor. Image taken from [68]	29
2.5	The constraints from a global fit to neutrino oscillation data[68] with an assumption of unitarity (black dotted) or no assumption of unitarity (red solid). The first two rows show little change from the unitarity assumption, indicating strong constraints from direct measurements. The elements of the third row, related to the ν_τ , show much larger changes, indicating that constraints are obtained from indirect oscillation measurements.	30
3.1	The IceCube DOM contains multiple components, including the PMT itself as well as various electronics necessary for semi-autonomous operation.	32
3.2	Afterpulsing calibration measurements performed in the lab. LEDs with known brightness were flashed to test for offtime response of the IceCube PMT. Clear dips, corresponding to detected charge, are visible. Drop (a) corresponds to the initial LED flash while (b), (c), and (d) show prominent afterpulsing peaks. Image taken from [69].	33

3.3 Examples of the ATWD (top) and FADC (bottom) waveforms output from an IceCube PMT. Taken from [37]	34
3.4 A histogram of the time between subsequent hits on DOM 15 of string 27. Hitspool data, specialized data collected with no trigger applied, is shown in blue. The "correlated" (non-Poissonian) and "uncorrelated" (Poissonian) features are shown in red and black respectively. The location of a large afterpulsing peak is shown in yellow. Note that the features included are not to scale. Image taken from [37].	35
3.5 The IceCube Neutrino Observatory. Three separate subdetectors are shown: IceTop, a cosmic ray air shower detector; IceCube, an array designed to search for astrophysical neutrinos; and DeepCore, a dense subarray optimized for atmospheric oscillation physics measurements. The detector was deployed over multiple years. Strings deployed in the same year are shown with identical colors at the surface.	36
3.6 A comparison of the standard IceCube string (right) to the DeepCore string (left). The IceCube string uses DOMs spaced 17 m apart while DeepCore divides the DOMs into a fiducial (bottom) and veto plug (top). The dust concentration is shown in red. The concentration of dust in the ice affects the scattering and absorption of the glacial ice.	37
3.7 Examples of event topologies above 1 TeV using the full IceCube array. Event views shown in (a) and (b) are from actual events discovered by the IceCube detector [77]. Images taken from [78]. (a) ν_e CC and ν NC show similar behavior from electromagnetic and hadronic interactions, which result in a shower of particles that quickly scatter in the ice. Cherenkov emission from these events appears roughly spherical in the detector. These events are known as "cascades". (b) ν_μ CC events begin with a hadronic interaction, then produce Cherenkov light from the outgoing muon. Above 1 TeV, the track of the outgoing muon becomes clearly visible. (c) Above 10 TeV, the tau lepton from a ν_τ CC may travel a significant distance before decaying. This results in two well-separated cascades in the detector, a tell-tale signature of ν_τ CC interactions.	38
3.8 A selection of 50 GeV simulated events in DeepCore taken from [78]. Unlike the event topologies at high energies, DeepCore events do not show distinct event types.	39
3.9 The data from the dust loggers deployed in various drill holes in IceCube during deployment. Data from individual holes has been offset in the y direction for clarity. Larger relative values of the "Optical Signal" represent more scattering in the ice while smaller values indicate clearer ice. The "dust layer" is visible in all drill holes around 2000 m. Deepcore DOMs are deployed below this layer. Image taken from [86].	39
3.10 The absorption and effective scattering properties of the ice as fit to flasher data. Two models are shown representing different generations of ice models used for simulation. The "Mie" model does not include anisotropy while the "Lea" model does. Figure from [87].	40

3.11	The effect of the anisotropy on the light output from a flasher on string 63. Measurements (points) are shown for receiving DOMs at three distances: at 125 m (red), at 217 m (blue), and at 250 m (green). A line is included to show the expected effect of anisotropy at each distance. The y-axis shows the ratio of a simulation of the same flasher without including anisotropy to data. A modulation is observed as a function of direction in the x-y plane. . .	41
4.1	Average energy losses ($\frac{-dE}{dx}$) for a muon in ice. At very low energies, ionization losses dominate. Above approximately 1 TeV, pair production and photonuclear effects become more important. Image taken from [21]	47
4.2	Examples of the angular acceptance models used by IceCube. The relative sensitivity as a function of arrival direction is shown with $\cos(\eta)= -1$ indicating the back of the PMT and $\cos(\eta)=1$ the face. The variation of the acceptance model used for this search is shown using by varying two parameters in the model. The 'p' parameter primarily controls the acceptance at the side of the DOM while the 'p2' parameter controls the acceptance from the forward region. A second model, H2, is also shown. . .	48
7.1	The FirstHit Z position	58
7.2	Number of Hits Above Z=-200	59
7.3	QR6 and C2QR6	59
7.4	Tensor-of-Inertia Eigenvalue Ratio	60
7.5	The improvedLineFit Speed	61
7.6	The L4 BDT Score	61
7.7	Time to 75% Charge	62
7.8	Veto Identified Causal Hits	63
7.9	First Hit ρ Position	63
7.10	Quartile Distance	64
7.11	Quartile Z-Travel	64
7.12	SPE Reconstruction Zenith Angles	65
7.13	The L5 BDT Score	65
7.14	Fill-Ratio	66
7.15	The NChannel Distribution	67
7.16	CorridorCut Distribution	68
7.17	The FiniteReco Containment Cuts	69
8.1	The sensitivity of this analysis in the (a) NC+CC and (b) CC-only channel. The top plot shows the Asimov expectation (black dotted line) and the Brazilian flag (green, yellow bands). The significances assuming Wilk's theorem (gray horizontal lines) and Feldman-Cousins (red horizontal lines) are also shown. The bottom plot shows the expected 1σ and 90% ranges for Wilks theorem and Feldman-Cousins compared to the most recent results from the OPERA and Super-Kamiokande analyses.	90
8.2	The test statistic distributions for 11 points in N_τ^{True} in the NC+CC fit. The assumption of 1 degree of freedom from Wilk's theorem is tested by looking at the location of $(\Delta\chi^2_{FS})_{90\%}$ for each point. The distribution calculated from Monte Carlo trials is narrower than that predicted by Wilk's theorem, indicating that a more complete treatment with the Feldman-Cousins procedure is necessary.	93

8.3	A comparison of the charge extraction in data and simulation at GRECO L7. Both the time and charge are shown for individual pulses on all DOMs. The time is measured relative to the largest pulse observed on each DOM during an event. The data and simulation histograms are independently normalized to 1.0. While the two show broad agreement, notable differences occur at low charge.	97
8.4	The reconstructed Z position using PegLeg. The GRECO L7 cuts have not been applied in order to show discrepancies below the detector. Noticeable disagreement is seen around a depth of $z=-450$	99
8.5	The reconstructed Z position plotted against the reconstructed distance from string 36. The L7 cuts from GRECO have been removed for this plot. The colorbars in both plots have been normalized to be identical. The data and simulation show reasonable agreement except for two points in the data, near $\rho_{36} = 75$ at depths of -310 and -490.	100
8.6	The reconstructed X position and Y position of events in the detector. The L7 cuts from GRECO have been removed for this plot. The colorbars in both plots have been normalized to be identical. Once again, reasonable agreement is observed in most regions, although data events have a clear excess near $x=110$ m, $y=-60$ m. This position corresponds to string 83.	100
8.7	The RMS of the charges within each event at final level. The value of the RMS is normalized using the total charge observed. The L7 cuts from GRECO are not applied here. The events with flaring DOMs cluster at high values of the charge RMS, visible in the inset.	101
8.8	The value of each systematic with priors. The best-fit values are shown for each while the priors are shown by the yellow band. The CC and NC+CC fits are highly correlated, as expected, with very little difference in the systematics best-fit values. All values fit well within the expected 1σ ranges.	103
8.9	A comparison of the posterior expected from trials to the final data fit value for each parameter for the CC-only fit. The trials used to build the posterior distribution in each parameter assume baseline values for systematics, $N_\tau^{CC} = 1$, and Nu-Fit 2.2 values [57]. The green vertical line shows the true injected value. The blue dotted line shows the best-fit value from data. The black bar shows the 1σ and 90% ranges calculated from the posterior distribution.	104
8.10	A comparison of the posterior expected from trials to the final data fit value for each parameter for the NC+CC fit. The trials used to build the posterior distribution in each parameter assume baseline values for systematics, $N_\tau^{NC+CC} = 1$, and Nu-Fit 2.2 values [57]	105

List of Tables

1.1	The branching ratios for the decay of tau leptons. Two-thirds of the time, the tau lepton decays hadronically.	17
-----	--	----

7.1	The FiniteReco containment cut for each of the channels. The cut itself is shown with the black line.	70
7.2	The PegLeg L7 containment cut for each of the channels. The cut itself is shown with the black line. Note that the atmospheric muons are here represented by the higher-statistics MuonGun sample.	72
7.3	The final two cuts applied to the sample prior to the analysis binning. All events are included here, although each cut is only applied to events with fewer than 14 hit DOMs. Note that the total simulation rate is scaled downward by 20% to approximately match the rate of the data events.	73
7.4	The event rates at each cut level in the GRECO selection. Note that the MuonGun events are included in this table, but do not contribute to the total Monte Carlo expectation to prevent double-counting of muon events from the CORSIKA sample. All rates are given in millihertz.	73
7.5	The true neutrino energy and zenith of the GRECO sample at final level. The sample shows an asymmetry between upgoing ($\cos(\theta) < 0$) and downgoing ($\cos(\theta) > 0$) event rates in the neutrinos due to selection bias. The sample has a long tail of events at both high and low energies. Using the NuFit 2.2 oscillation parameters and the flux model from Honda, the ν_τ events are observed in the very upgoing region around $10^{1.4} = 25$ GeV.	74
7.6	The reconstructed energy and zenith of the GRECO sample at final level. Events in data reconstruct to both relatively high energies ($E_R > 100$ GeV) and very low energies ($E_R \approx 2$ GeV). Using the NuFit 2.2 oscillation parameters and the flux model from Honda, the ν_τ events are observed in the very upgoing region around $10^{1.4} = 25$ GeV.	75
8.1	The rates expected for each of the neutrino types in the Super-Kamiokande search for ν_τ appearance. Reproduced from.	79
8.2	Total χ^2 impact of each of the oscillation parameters. The atmospheric mixing parameters, Δm_{31}^2 and θ_{23} are the most important oscillation parameters for the GRECO selection. Of the remaining parameters, the CP-violating phase is the next most important.	80
8.3	Systematics sets used for the characterization of the signal neutrino events. While all listed sets have up to 30 years of effective livetime available, not all events are processed in each set.	81
8.4	Systematics sets used for the characterization of the atmospheric muon background.	82
8.5	Priors and allowed ranges for each systematic included in this analysis.	88
8.6	The best-fit systematics values for each nuisance parameter in the fit. The corresponding parameters for $N_\tau = 1$ (ie, the disappearance fit) are included for reference. The CC-only and NC+CC fits are highly correlated, as expected.	106

Introduction

Measurements of atmospheric neutrino oscillations, such as those performed in this thesis, require a background of understanding of both atmospheric neutrinos as well as neutrino oscillations. A history of neutrinos (Section 1) is used to explain the discovery of the three known flavors of neutrinos as well as the difficulties inherent in the study of these elusive particles. A discussion of the history of cosmic rays (Section 1.1) explains the source of both the neutrinos (Section 1.2) used as signal in this thesis as well as the muons, which form one of the primary backgrounds in the search for atmospheric oscillations.

The detection of neutrinos is described in two parts. A discussion of the neutrino interactions (Section 1.4), explains the interactions of neutrinos with matter. The detection of these interactions through electromagnetic emission is then covered (Section 1.4.1).

1.1 The History of the Neutrino

In 1896, Henri Becquerel discovered radioactivity in uranium [1]. Measurements over the following decades showed various types of nuclear decays based on the penetration depth of the ionizing emissions. Measurements of one type of radioactivity, the beta decays, over the following 30 years showed that the production of two observed particles from one parent nucleus: a daughter nucleus and an outgoing electron. A single body decay of this type produces a known spectrum due to conservation of energy and momentum. The energy of the daughter nucleus and the electron are completely determined by these two conditions, leading to a narrow line emission spectrum.

Contrary to expectations, however, the measurement of energies of the two resulting particles showed wide, continuous spectra [2]. The spectrum provided a major puzzle for physicists due to the contradiction with the simple theoretical expectations. A conundrum for many years, one possible solution was suggested in 1930 by Wolfgang Pauli. In his letter, Pauli suggested that the conservation of energy and momentum could be saved if "... there could exist in the nuclei electrically neutral particles... which have spin 1/2 and obey the exclusion principle, and additionally different from light quanta in that they do not travel with the velocity of light" [3]. The solution to the beta decay puzzle was, then, that this additional "neutron" particle was emitted simultaneously with the observed daughter particles. This newly proposed particle would be electrically neutral and, therefore, unable to be seen through traditional methods. The resulting spectrum of the observed particles could then be continuous, as verified experimentally.

Pauli's suggestion provided a way to save the beloved conservation laws in physics, but at the expense of the assumption of a new particle. The particle, called the "neutron" in Pauli's letter and later renamed the "neutrino" by Fermi, was proposed to be electrically neutral and, therefore, completely undetectable at the time. Later work proposed that the neutrinos interact only via the weak nuclear force, with an interaction strength many orders of magnitude smaller than electromagnetic and strong nuclear forces. Experimental measurements, sensitive only to electromagnetic forces, therefore cannot be used to study neutrinos directly in the same way that other particles may be measured.

It was not until nearly 20 years later, in 1956, that this mystery particle was first detected [4]. In a groundbreaking work, Cowen and Reines presented an experiment at the Savannah River Plant, a nuclear power plant, demonstrating detection of the neutrino. The experiment, made up of layers of scintillation detectors around polyethelene boxes,

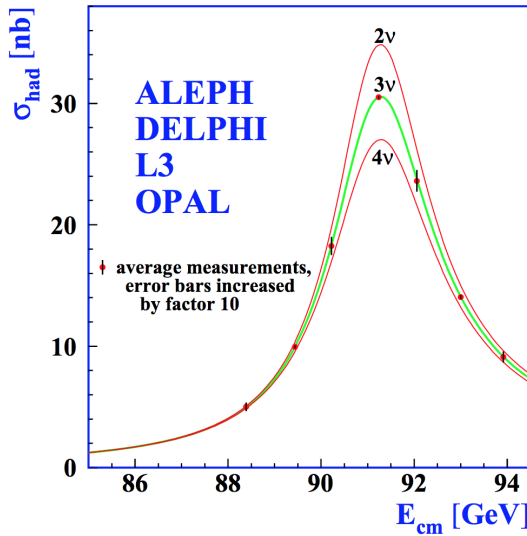


Figure 1.1 – The number of active neutrinos as measured by ALEPH, DELPHI, L3, and OPAL. The data from the four experiments strongly favors only three neutrinos coupling to the Z boson. Image taken from [9].

yielded a signal-to-background rate of about 3 to 1 with a rate of 2.88 ± 0.22 counts/hour with a total livetime of 1371 hours, including time during which the nearby nuclear reactor was offline. For the discovery of the first neutrinos, Frederick Reines was granted a shared Nobel Prize in Physics for the year 1995 [5].

Since the neutrino was first observed, additional measurements have discovered two new flavors of neutrinos: the muon neutrino [6] and the tau neutrino [7, 8].

Searches for additional neutrinos beyond the discovered three have been performed by investigating the decays of the Z boson. The Z boson, a particle of 91 GeV [pdg], couples both to the neutrinos and to more easily observed hadrons and charged leptons making it a useful probe of neutrino interactions. The width of the Z decay to hadrons, for instance, is affected by the number of active, light neutrino species [9]. Additional flavors of neutrinos coupling to the Z boson would lead to a smaller decay rate to hadrons observed in accelerator searches for hadrons as shown in Figure ???. The number of neutrinos may be calculated by comparing the best-fit ratio of "invisible" decays of the Z boson (ie, those involving two neutrinos) to the measured width expected from charged leptons in the standard model.

$$R_{inv} \equiv \frac{\Gamma_{inv}}{\Gamma_{ll}} = N_\nu \left(\frac{\Gamma_{\nu\nu}}{\Gamma_{ll}} \right)_{SM} \quad (1.1)$$

Here the number of neutrinos is extracted by assuming that all active neutrinos have the same coupling to the Z boson, result which has been verified experimentally. A precision measurement of the Z resonance completed at the LEP collider found the best fit value of $N_\nu = 2.9840 \pm 0.0082$, in good agreement with only three active neutrinos.

1.2 History of Cosmic Rays

In the early years of the 20th century, scientists began investigating previously-unknown ionizing radiation in the atmosphere. Scientists using electroscopes, early instruments designed to measure electric charge and radiation, discovered low levels of radiation

in the air. This new radiation was observed to be reduced when the electroscope was shielded by metal free of radioactivity, indicating that the signal was not an artifact of the detector itself and was, instead, coming from an external source.

Following just a few decades after the discovery of radioactivity by Becquerel, many scientists believed that the electroscope was picking up radiation from the Earth itself. The rate would be expected to decrease with increasing altitude above sea level and, to increase with increasing depth in the sea. Early measurements by Domenico Pacini in 1910 showed that the radiation rate decreased by 20% at a depth of 3 meters underwater compared to the rate at the surface [10], implying an origin independent of the Earth's crust. Measurements were performed with electroscopes by Victor Franz Hess in 1912 of the rate of ionizing radiation up to an altitude of 5 km [11].

Hess showed that the observed rate decreased until an altitude of around 1 km, but at a slower rate than expected from theory. Above 1400 meters, however, the rate of ionizing radiation increased again, rising substantially up to the maximum altitude reached at 5300 meters [12]. Hess's work, later confirmed by Henri Millikan, showed definitively that there exists a source of radiation of extraterrestrial origin, earning him the Nobel Prize in Physics for 1936 [13]. This radiation was later dubbed "cosmic rays" by Millikan in reference to their extraterrestrial origin.

Work on cosmic rays has lead to numerous discoveries. In 1937, the first *hadronic showers* were observed [14]. Hadronic showers of particles created by interactions of cosmic rays were shown to produce large numbers of particles [15, 11], with many producing from 5×10^6 to over 10^9 particles [16]. These showers begin with a cosmic ray primary particle, often a single proton accelerated to high energies, which interacts with particles of the Earth's atmosphere. The interaction leads to the creation of various daughters, including neutrinos, muons, pions, kaons, and other hadrons.

Modern measurements have shown that the cosmic ray spectrum primarily consists of protons with a small contribution from helium and heavier elements [17]. These ions are accelerated in unknown astrophysical sources up to extremely high energies. The cosmic ray spectrum extends over many orders of magnitude, with the highest energy observations reaching 10^{20} electronvolts - far higher than any Earth-based accelerator. The spectrum, shown in Figure 1.2, has multiple features that are believed to arise from different accelerator sources at different scales, each of which has been verified by multiple experiments.

1.3 Atmospheric Neutrinos

Air showers from cosmic rays provide a useful natural source of neutrinos in the GeV energy range and above that may be used for fundamental physics research. The hadronic shower produces pions and kaons which, in turn, decay to produce neutrinos

$$\pi^+ \rightarrow \mu^+ \nu_\mu \rightarrow e^+ \nu_e \bar{\nu}_\mu \nu_\mu \quad (1.2)$$

from the pions and from the kaons

$$K^+ \rightarrow \pi^+ \nu_\mu \rightarrow e^+ \nu_e \bar{\nu}_\mu \nu_\mu \nu_\mu \quad (1.3)$$

The neutrino flux depends on a number of parameters, including the Earth's magnetic field and temperature profile, the cosmic ray flux, and the details of hadronic interactions in air showers [18]. The calculation of the neutrino flux predictions requires significant, dedicated simulation work, producing fluxes as both a function of energy (Figure 1.3) and direction (Figure 1.4).

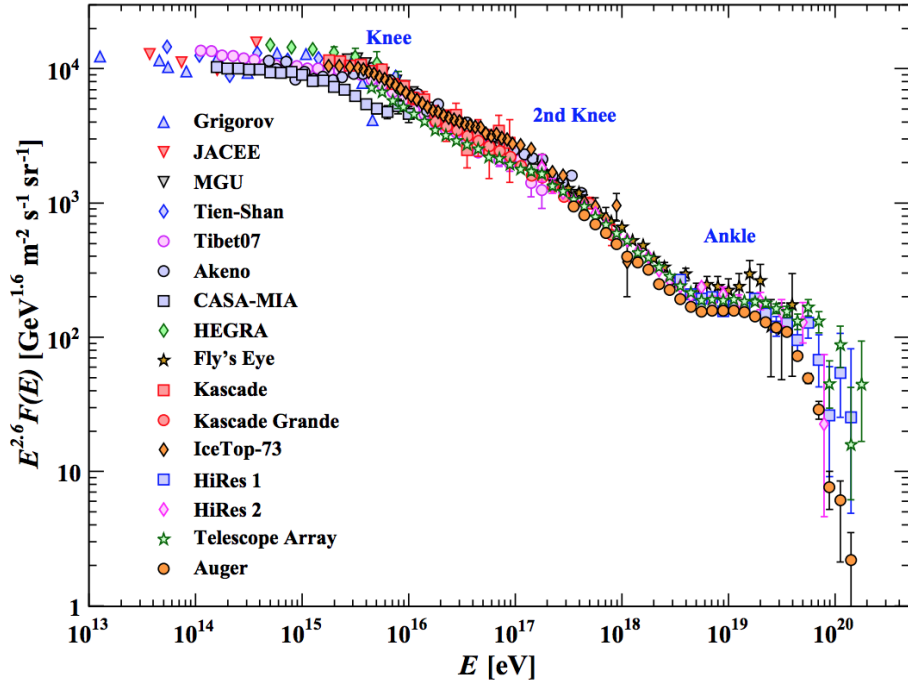


Figure 1.2 – The cosmic ray spectrum covers many orders of magnitude and has been verified by many experiments to high precision. The various features are thought to be caused by multiple sources at different scales. Image taken from [17]

1.4 The Standard Model

Muons and neutrinos form just a small part of the Standard Model of particle physics. The Standard Model, with fundamental particle types and properties shown in Figure 1.5, consists of six quarks (up, down, strange, charm bottom, and top), three charged leptons (electron, muon, tau), three uncharged leptons (electron neutrino, muon neutrino, and tau neutrino), and the five bosons related to interactions (photon, Z, W, gluon, and Higgs). Combinations of the quarks lead to various hadrons, particles which interact with and are formed via the strong force, with different combinations of quarks and anti-quarks producing a wide variety of particles. The Standard Model, developed over the last half century, elegantly encapsulates the range of phenomena known to occur in particle physics and has been verified repeatedly over decades by many experiments. Predictions of the Standard Model have been carefully verified by accelerator experiments, yielding precise checks on a wide range of parameters.

The three charged leptons and neutrinos form three "families" or "flavors". Each charged lepton possesses a coupled neutrino which shares a lepton number conserved in interactions. The electron, the lightest of the charged leptons at 511 keV [17], is a key ingredient of the atoms that make up the world, forming the basis for all of chemistry and is the only stable charged lepton. The muon, with a mass of 105.7 MeV, is the middle of the three charged leptons, often appearing in particle interactions accompanied by the muon neutrino. The muon has a relatively long lifetime of 2.197 microseconds, far longer than many unstable hadrons. The tau lepton is the heaviest of the leptons, and with a mass of 1.777 GeV, it is heavier than the proton and appears only in relatively high energy interactions. The tau has an extremely short lifetime, at 290.6 femtoseconds, and a rich

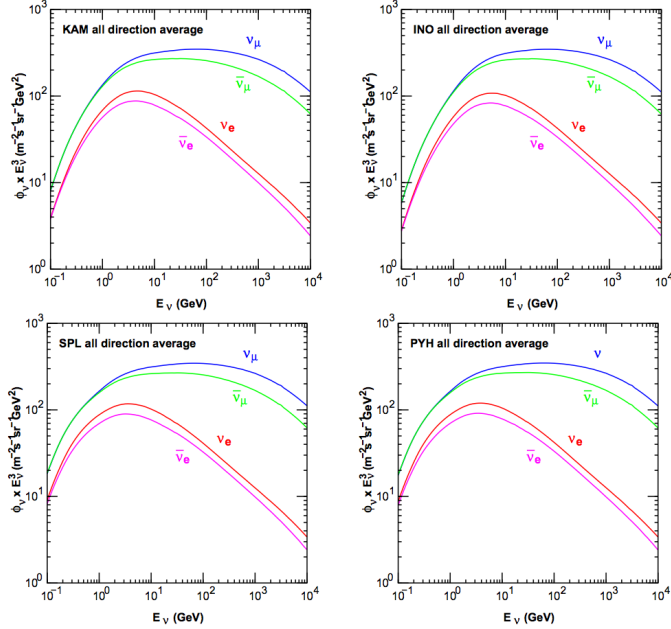


Figure 1.3 – The expected neutrino flux at Kamioka mine, Japan (Super-Kamiokande, top left), Ino Peak, India (India-based Neutrino Observatory, top right), the South Pole (IceCube, bottom left), and Pyhasalmi mine, Finland (EMMA experiment, bottom right) as a function of energy. Note that the neutrino and anti-neutrino fluxes are characterized separately. The differences in the flux at each site is due to differences in the Earth’s magnetic field and temperature profile. Figure taken from [18].

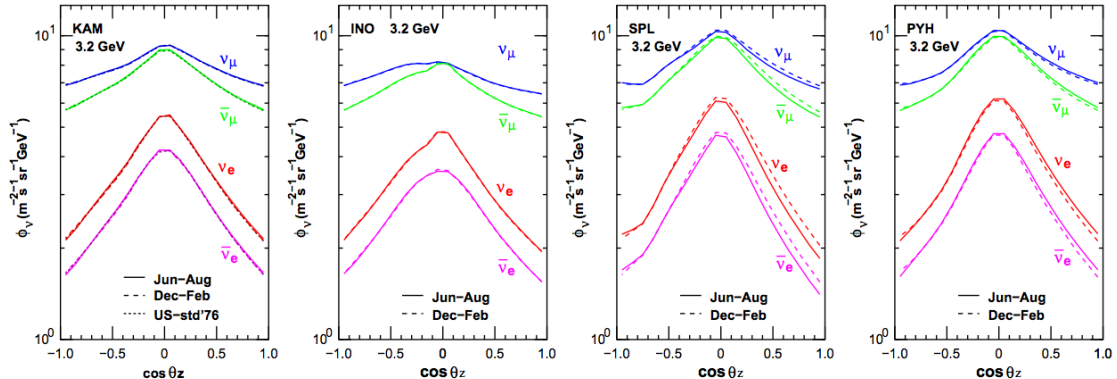


Figure 1.4 – The expected flux of 3.2 GeV neutrinos at Kamioka mine, Japan; Ino Peak, India; the South Pole; and Pyhasalmi mine, Finland as a function of zenith angle. A value of $\cos \theta_Z = -1$ indicates neutrinos passing through the entire Earth and entering the detector from below while a value of $\cos \theta_Z = +1$ indicates neutrinos interacting in the atmosphere directly above the detector. The differences in the flux at each site is due to differences in the Earth’s magnetic field and temperature profile. Figure taken from [18].

variety of decay products. This extremely short lifetime and high mass make the tau difficult to produce and study.

For the purposes of this work, the most significant parts of the Standard model are the neutrinos, which will be defined to be signal events; the up and down quarks, which will make up the protons and neutrinos upon which the neutrinos will interact; the W and Z

Standard Model of Elementary Particles

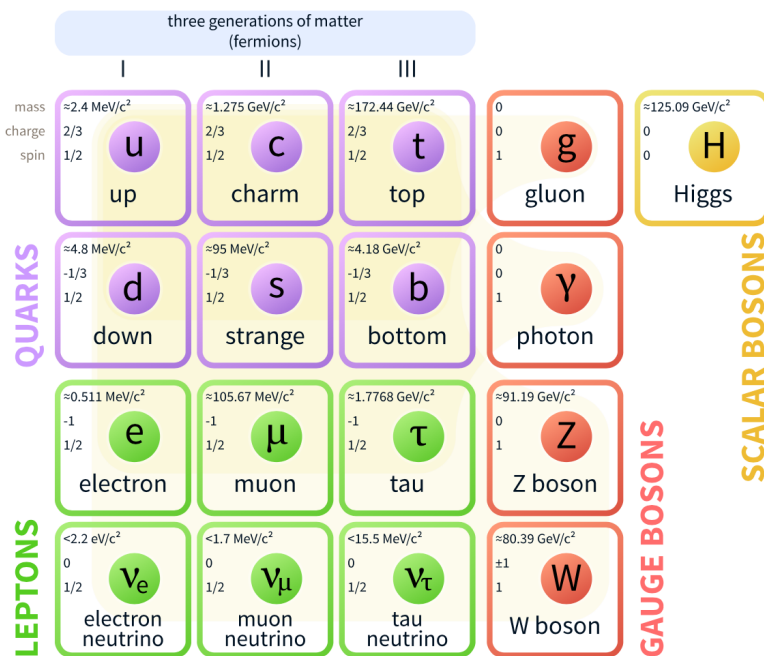


Figure 1.5 – The Standard Model of particle physics is made up of charged and uncharged leptons, quarks, and the various bosons. Image taken from [19]

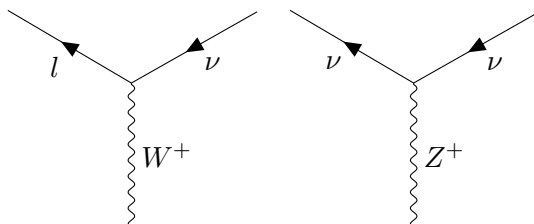


Figure 1.6 – Feynman diagrams showing the interaction vertex of the neutrino with the W and Z boson.

bosons, which mediate the weak interactions via which the neutrinos may be observed; and the photon, which gives a method of observation of the interactions.

1.4.1 Neutrino Interactions

In the Standard Model, neutrinos are assumed to be massless, left-handed spin-1/2 leptons which interact solely via the weak force. Neutrinos, therefore, are only visible via indirect effects, such as scattering or production of charged particles that may, in turn, give off their own visible signature. An understanding of the methods by which neutrinos are detected therefore forms an important basis for the study of these elusive particles. Two basic Feynman diagrams, shown in Figure 1.6, may be used to represent the interaction vertices available for neutrinos.

These two vertices describe the interactions relevant for the work presented in this thesis. During so-called *charged-current* (*CC*) interactions, a W^\pm boson is exchanged between a neutrino and target particle, in the process converting the uncharged neutrino to the corresponding charged lepton. The *neutral-current* (*NC*) interactions are those in which

the uncharged Z boson is exchanged with the target and the neutrino, although losing a fraction of the initial energy, does not get converted to a charged lepton.

Detectors used to study particle properties rely on electromagnetic interactions and photons in order to detect particles. Because the neutrino itself does not interact via the electromagnetic force, charged leptons and hadrons must be used to indirectly study the properties of the incident neutrinos. Outgoing charged leptons in charged-current interactions may be detected, although the direction will not necessarily correspond to that of the incident neutrino. The average angle between the incident neutrino and outgoing lepton may be approximated following Equation 1.4.

$$\bar{\theta}_{\nu l} \approx \frac{1.5^\circ}{\sqrt{E_\nu [TeV]}} \quad (1.4)$$

There exist three further classifications of neutral-current and charged-current neutrino interactions in the energy range used in this work: the quasi-elastic, resonant, and deep inelastic interactions [20]. A fourth type, coherent neutrino scattering, may also occur, although the energies involved are too low to impact this work. The three types of interactions contribute to the total cross-section with peaks at different energies, as shown in Figure 1.7.

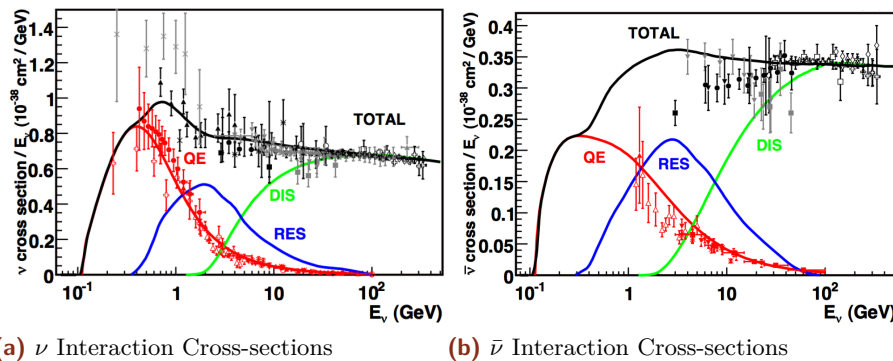


Figure 1.7 – The relative contributions to the cross section for ν (left) and $\bar{\nu}$ (right). The QE events dominate below 1 GeV while the DIS events dominate above 10 GeV. Note the different scales for the neutrino and antineutrinos. Images taken from [20]

lofsubfigure\numberline(a)\nu Interaction
Cross-sections
Cross-sectionslofsubfigure\numberline(b)\mathaccen{V}{\bar{0}}{16}\nu Interaction
Cross-sections

Quasi-Elastic and Resonant Interactions

At low energies of approximately 100 MeV to around 2 GeV, the neutrinos interact via *quasi-elastic scattering (QE)* interactions. In the QE interaction, the neutrino scatters off an entire nucleon instead of the individual quarks. In a charged current QE neutrino (anti-neutrino) interaction, the target neutron (proton) is converted to a proton (neutron) while the neutrino is converted to a charged lepton.

The cross section for QE interactions depends on various nuclear form factors that must be fit to experimental data. Many of these form factors may be fit to electron scattering

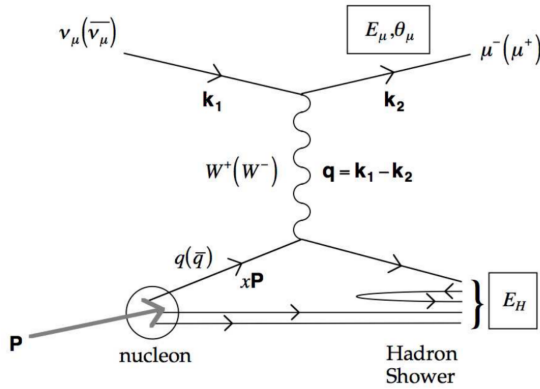


Figure 1.8 – A Feynman diagram showing an example of a CC neutrino DIS interaction. An incident muon neutrino interacts with a quark inside of a proton. The result is a hadronic shower as well as a charged muon. Diagram taken from [formaggio-xsec]

data, leaving only the axial vector nuclear form factors to be measured in the neutrino sector [20]. This form factor is normally assumed to have the dipole form

$$F_A(Q^2) = \frac{g_A}{\left(1 + \frac{Q^2}{M_A^2}\right)^2} \quad (1.5)$$

where g_A is a constant fit to experimental data, Q^2 is the 4-momentum transferred in the interaction, and M_A is the "axial mass". This last term is fit to experimental data with a value of $M_A = 0.999 \pm 0.011$ GeV [20].

Resonant scattering interactions (*RES*), which result in the excitation of a nucleon followed by decay via emission of (typically) pions, occur for neutrinos of slightly higher energies of around 500 MeV to 10 GeV. Resonant interactions are modeled in a similar way as the quasi-elastic interactions, with an associated axial mass term used to describe nuclear uncertainties.

Deep Inelastic Interactions

Above a few GeV, the neutrino cross section rises approximately linearly with energy and is dominated by *deep inelastic scattering (DIS)* interactions. An example of a DIS interaction is shown in Figure 1.8. In DIS events, the exchange of the Z or W boson probes the internal structure of the nucleons, leading to a scattering off of the individual quarks of the nucleus. This results in disruption of the nucleon and the larger nucleus and a collection of daughter particles forming a *hadronic shower*.

As seen in Figure 1.7, the DIS events dominate the neutrino cross section above 10 GeV and form the only significant interaction above 100 GeV [formaggion-xsec]. Experiments with high statistics samples of DIS events have been used to measure the charged current cross section to the few-percent level.

1.5 Methods of Detection

Neutrinos may be detected through the QE, RES, and DIS interaction channels, with each possessing a distinct signature. The interaction of neutrinos at the GeV energy ranges relevant for this thesis lead to the emission of hadrons in a hadronic shower. The lower energy QE and RES interactions typically yield only one pion which may decay into

Decay	Branching Ratio	Background
$\tau \rightarrow e^- \nu_e \nu_\tau$	$17.83 \pm 0.04 \%$	ν_e CC
$\tau \rightarrow \mu^- \nu_\mu \nu_\tau$	$17.41 \pm 0.04 \%$	ν_μ CC
$\tau \rightarrow \text{hadrons}$	Otherwise	ν NC

Table 1.1 – The branching ratios for the decay of tau leptons. Two-thirds of the time, the tau lepton decays hadronically.

a pair of photons (π^0) or into further charged hadrons and leptons (π^\pm). DIS interactions produce larger hadronic showers containing many charged particles that may be detected. In addition to the hadronic shower, charged-current interactions result in an outgoing charged lepton, the result of which depends on the flavor of the incident neutrino. Outgoing electrons quickly scatter in interactions with the surrounding media, ionizing atoms and producing a secondary *electromagnetic shower* of particles. Muons, on the other hand, travel longer distances before scattering or decaying in the medium, leading to an extended track.

The signature of a tau neutrino charged current interaction varies depending on the specific decay channel of those presented in 1.1. Because the tau lepton has a very short lifetime, outgoing taus tend to decay immediately, producing daughter particles. Each of the three decay modes mimic interactions of the electron and muon neutrinos. The secondary electromagnetic or hadronic cascade is theoretically distinguishable from the primary hadronic cascade produced by a tau neutrino charged current interaction, although the distance traveled by the tau lepton at the energies relevant for this work is on the order of millimeters, far below the reconstruction precision possible with the IceCube detector.

In each case, the charged particles deposit energy into the interaction medium during travel through a series of stochastic and continuous emissions. It is through the detection of these stochastic and continuous losses that daughter particles may be identified in the study of neutrinos.

1.5.1 Stochastic Emission Mechanisms

A total of five major stochastic emission mechanisms are important for the energy losses in neutrino experiments [21]. One such mechanism is the decay of the particle, a process which splits the energy of the parent into multiple, lower energy daughters. Decays of daughter leptons can often be important in the identification of the neutrino flavor, particularly for tau neutrino candidates occurring above 10 TeV when the primary and secondary hadronic interactions become well-separated.

Ionization losses occur when the charged lepton interacts with electrons in the medium, transferring enough energy to liberate the electrons from bound states. At energies below 1 TeV, these losses are the most significant form of energy loss for charged particles, producing a significant source of additional electrons. Ionization losses occur roughly independently of the energy of the charged lepton.

Above energies of a few hundred GeV, radiative processes dominate the energy losses for muons in matter [17]. Bremsstrahlung, photon emission from charged particles accelerating in a magnetic field, pair production, in which a particle and antiparticle (typically electron and positron) are created, and hadronic interactions of photons all dominate the energy losses of muons above 1 TeV.

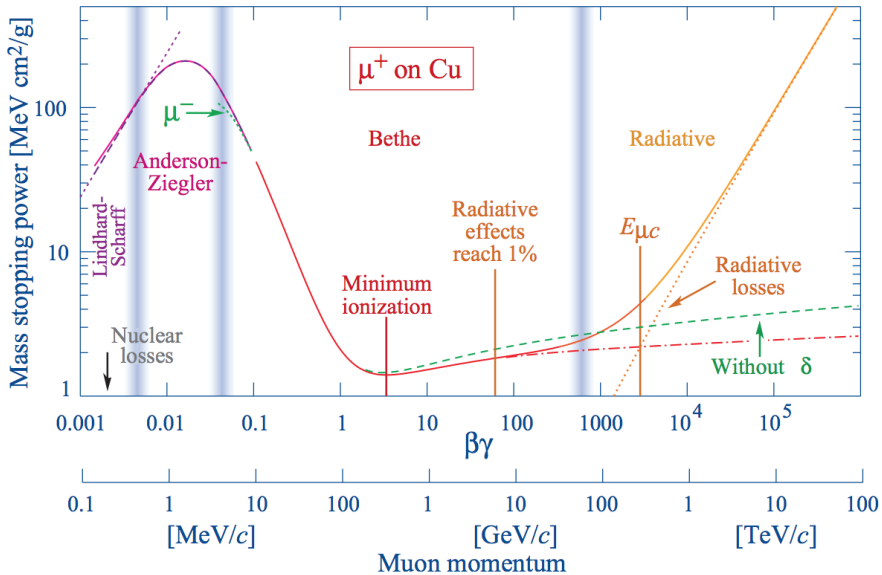


Figure 1.9 – An example of the energy loss ($-\frac{dE}{dx}$) calculated for muons incident on copper. Note the radiative losses due to bremsstrahlung, pair production, and photonuclear interactions above 1 TeV. Note also the labeled minimum demonstrating the energy of a minimum ionizing particle. Image taken from [17].

There exists a minimum in the energy loss rates. Particles emitting near this minimum rate are known as *minimum-ionizing* particles [17].

Stochastic emissions result in additional particles in the detector, leading to improved light yield. In addition, some detectors use photosensitive emulsions [22, 7], scintillators [23, 24, 25, 26], or time projection chambers [27] in order to track ionization losses. These emulsions yield precise characterization of particle decays, allowing experimentalists to uniquely determine the flavor state of the interacting neutrino.

1.5.2 Cherenkov Emission

When a charged particle passes through a dielectric medium with a speed larger than the local phase velocity of light, it will emit *Cherenkov radiation* [28]. The effect, first reported by Pavel Cherenkov in 1934 [29] remained unexplained theoretically until work done by Ilya Frank and Igor Tamm in 1937 [30].

For a dielectric medium, the electric field of the charged particle will polarize atoms by inducing a small dipole moment due to electromagnetic effects in nuclei of atoms in the medium [31]. The resulting disturbance of the medium propagates with the phase velocity of light, given by the speed of light, c , and the index of refraction as a function of the frequency of light, $n(\omega)$. If the charged particle is traveling faster than the local phase velocity, the electromagnetic disturbance propagates with constructive interference, resulting in a planar wavefront of emission known as *Cherenkov emission*. The angle of the wavefront relative to the propagation direction is given by the ratio of the distance traveled by the particle and photons in a given time.

$$\cos(\theta_C) = \frac{\frac{c}{n(\omega)}t}{vt} = \frac{c}{n(\omega)v}, \quad (1.6)$$

The energy threshold for Cherenkov emission is set by a combination of the particle mass and the local phase velocity for light, $\frac{c}{n}$. Using the relativistic kinetic energy [32],

$$E_C \geq \frac{mc^2}{\sqrt{1 - \left(\frac{c/n}{c}\right)^2}} \quad (1.7)$$

$$E_C \geq mc^2 \sqrt{\frac{n^2}{n^2 - 1}} \quad (1.8)$$

For ice with a index of fraction of 1.32 at 400 nanometers [33], this works out to a minimum energy of 270 keV for electrons and 56.2 MeV for muons. The number of photons emitted increases with energy, with approximately 50% more photos produced in blue visible light than in red[32] The full emission spectrum, first worked out by Ilya Frank and Igor Tamm in 1937 [30], depends on a number of parameters, including the energy and charge of the emitting particle as well as the properties of the medium. In the case of a particle traveling a distance L much larger than the photon frequency of interest, λ , the number of emitted photons may be approximated by

$$\frac{dN}{d\lambda} = \frac{2\pi\alpha}{\lambda^2} L \sin^2\theta_C \quad L \gg \lambda \quad (1.9)$$

Cherenkov emission is not limited to a single charged lepton. All charged particles emit Cherenkov radiation, including any hadrons and charged daughter particles, resulting in measurable signals. While the total amount of energy lost via Cherenkov emission is small relative to losses due to stochastic processes, this emission type is both continuous and results directly in photons which may be observed by photodetectors. This technique is used by multiple experiments, including SNO [34], Super-Kamiokande [35], ANTARES [36], and IceCube [37].

Neutrino Oscillations

The search for oscillation events requires an explanation of neutrino oscillations. The theory of neutrino oscillations is included here with broad descriptions of oscillations in vacuum (Section 2.1.1) and in matter (Section 2.1.2). Experimental evidence for the neutrino oscillations and current constraints on the oscillation parameters is presented in Section 2.1.3. Finally, a description of unitarity in the PMNS mixing matrix is given in Section 2.4.1 with particular emphasis placed on the search for additional neutrino flavors (Section 2.5). The motivation for this thesis as well as the purpose behind joint fits between appearance and disappearance data is discussed in Section 2.5.2.

2.1 Oscillation Theory and the PMNS Matrix

In 1968, Bruno Pontecorvo suggested a process, known as *neutrino oscillation*, by which neutrinos could change flavors [38]. The theory of neutrino oscillations was further developed for the neutrino sector by Ziro Maki, Masami Nakagawa and Shoichi Sakata in 1962 [39].

2.1.1 The PMNS Mixing Matrix

We now understand there to be three distinct flavors of neutrinos. Neutrinos are created via the weak force as pure flavor eigenstates. These states are coherent superpositions of mass eigenstates. Specifically, there exist three weak eigenstates of the left-handed neutrino fields that are related to three known neutrino mass eigenstates via the Pontecorvo-Maki-Nakagawa-Sakata (*PMNS*) lepton mixing matrix.

$$\begin{pmatrix} \nu_e \\ \nu_\mu \\ \nu_\tau \end{pmatrix} = U_{PMNS} \begin{pmatrix} \nu_e \\ \nu_\mu \\ \nu_\tau \end{pmatrix} = \begin{pmatrix} U_{e1} & U_{e2} & U_{e3} \\ U_{\mu 1} & U_{\mu 2} & U_{\mu 3} \\ U_{\tau 1} & U_{\tau 2} & U_{\tau 3} \end{pmatrix} \begin{pmatrix} \nu_1 \\ \nu_2 \\ \nu_3 \end{pmatrix} \quad (2.1)$$

The flavor eigenstates $(\nu_e, \nu_\mu, \nu_\tau)$ describe the fields of the left-handed neutrinos coupling via the weak charge to the electron, muon, and tau respectively. The three mass states (ν_1, ν_2, ν_3) represent the mass eigenstates. The mixing between the two types of states is given by the unitary matrix, U_{PMNS} . The mixing may be written in a shortened form

$$\nu_\alpha(x) = \sum_i U_{\alpha i} \nu_i(x) \quad (2.2)$$

where $\alpha = e, \mu, \tau$ and $i = 1, 2, 3$.

Neutrinos interact via the weak force and are created in flavor states e, μ, τ . The neutrino produced in flavor state ν_α exists in a superposition of the three mass eigenstates.

where δ_{ij} and $\delta_{\alpha\beta}$ are Kronecker delta functions. As a 3×3 unitary matrix, the PMNS matrix may be parametrized in terms of three mixing angles and six phases. Of these phases, five may be removed by rephasing the lepton fields with no change to the underlying physics, leaving one physical phase related to CP violation.

The PMNS may be written in terms of the product of three smaller unitary matrices using these mixing angles.

$$U_{PMNS} = \begin{pmatrix} 1 & 0 & 0 \\ 0 & c_{23} & s_{23} \\ 0 & -s_{23} & c_{23} \end{pmatrix} \begin{pmatrix} c_{13} & 0 & s_{13}e^{-i\delta_{CP}} \\ 0 & 1 & 0 \\ -s_{13}e^{i\delta_{CP}} & 0 & c_{13} \end{pmatrix} \begin{pmatrix} c_{12} & s_{12} & 0 \\ -s_{12} & c_{12} & 0 \\ 0 & 0 & 1 \end{pmatrix} \quad (2.3)$$

where the notation c_{ij} idenotes $\cos(\theta_{ij})$ and s_{ij} denotes for $\sin(\theta_{ij})$.

Note that if neutrinos are Majorana fermions, the additional phases may not be removed without making the masses complex. The Majorana terms form additional diagonal terms in Equation 2.3. While Majorana mass terms are beyond the scope of this work, further information may be found in [40, 41].

The three submatrices of Equation 2.3 have historically been studied by different types of experiments. This history has lead to the proliferation of alternative names for the matrices and of the mixing angles.

$$U_{PMNS} = U_{Atmospheric} U_{Reactor} U_{Solar} \quad (2.4)$$

This leads to the alternative names of the mixing angles, with θ_{23} , θ_{13} , and θ_{12} being referred to as the atmospheric mixing angle, the reactor mixing angle, and the solar mixing angle respectively.

2.1.2 Neutrino Mixing in Vacuum

Propagation of neutrinos requires the use of the Hamiltonian. However, the flavor states are not eigenstates of the Hamiltonian. For propagation of the neutrino, the mass eigenstates must instead be used.

$$|\nu(t=0)\rangle = |\nu_\alpha\rangle = \sum_i U_{\alpha i}^* |\nu_i\rangle \quad (2.5)$$

The propagation leads to a neutrino state at time $t \neq 0$ which is no longer a pure flavor state.

$$|\nu(t)\rangle = \sum_i U_{\alpha i}^* e^{-iE_i t} |\nu_i\rangle \quad (2.6)$$

where $E_i = \sqrt{p^2 + m_i^2}$ is the total energy of the i th mass eigenstate. If the neutrino state interacts, the flavor eigenstate must again be used to calculate the probabilities of interacting as each of the three known flavors.

$$P(\nu_\alpha \rightarrow \nu_\beta) = |\langle \nu_\beta | \nu(t) \rangle|^2 = \left| \sum_i U_{\beta i} U_{\alpha i}^* e^{-iE_i t} \right|^2 \quad (2.7)$$

Proper calculations from this point can be performed by treating each neutrino as a quantum mechanical wave packet [42]. This allows for the full description of neutrino oscillation in the context of decoherence of the mass states during propagation, allowing each mass state to possess separate momenta.

In practice, the description of neutrino oscillations necessary for this work is adequately described by making a few simplifying assumptions. In particular, this work assumes that all mass eigenstates propagate as plane waves possessing identical, well-defined momenta [40]. Neutrinos are further assumed to be extremely relativistic at the energies of interest, an assumption well-justified by cosmological fits to the sum of the three

neutrino masses, which give an upper limit of around 0.2 eV [17]. The total neutrino energy is also assumed to be unchanged during propagation. The resulting calculation of the oscillation probabilities is identical in both the simplified version and the full derivation.

To begin, equation 2.7 is expanded by explicitly including the complex conjugate,

$$P(\nu_\alpha \rightarrow \nu_\beta) = \sum_i^3 U_{\beta i}^* U_{\alpha i} \sum_j U_{\beta j} U_{\alpha j}^* e^{i(E_i - E_j)t} \quad \alpha, \beta = e, \mu, \tau. \quad (2.8)$$

In the highly relativistic limit, $E \gg m_i$, and $t \approx L$ where L is the distance traveled during propagation. Using these two approximations, the exponential term in Equation 2.7 may be rewritten using Euler's formula

$$e^{i(E_i - E_j)t} = 1 - 2 \sin^2 \left(\frac{m_{ij}^2 L}{4E} \right) + i \sin \left(\frac{m_{ji}^2 L}{2E} \right) \quad (2.9)$$

Note that a new shorthand has been defined, $\Delta m_{ji}^2 = m_j^2 - m_i^2$, giving a fundamental parameter of neutrino oscillations. The PMNS terms of equation 2.8 may be expanded further, yielding

$$\left| \sum_j U_{\beta j} U_{\alpha j}^* \right|^2 = \delta_{\alpha\beta} + 2 \sum_{i < j} \sum_i U_{\beta i}^* U_{\alpha i} U_{\beta j} U_{\alpha j}^* \quad (2.10)$$

where the factor of two arises due to the symmetry $i \leftrightarrow j$. Putting the terms together, the final oscillation probability formula is

$$P(\nu_\alpha \rightarrow \nu_\beta) = \delta_{\alpha\beta} - 4 \sum_{i < j} \operatorname{Re} \left[\sum_i U_{\beta i}^* U_{\alpha i} U_{\beta j} U_{\alpha j}^* \right] \sin^2 \left(\frac{m_{ij}^2 L}{4E} \right) + 2 \sum_{i < j} \operatorname{Im} \left[\sum_i U_{\beta i}^* U_{\alpha i} U_{\beta j} U_{\alpha j}^* \right] \sin \left(\frac{m_{ji}^2 L}{2E} \right). \quad (2.11)$$

This calculation has been derived for neutrinos. To calculate the probabilities for anti-neutrinos, the calculation changes by replacing $U \rightarrow U^*$, resulting in a change in sign of the last term of Equation 2.11.

From Equation 2.11, the general form of the oscillation probabilities becomes clear. The PMNS matrix elements yield the amplitude of oscillations, while the phase of the oscillations is related to three quantities: the squared difference in the masses, Δm_{ji}^2 ; the baseline, or distance traveled, L ; and the energy of the neutrinos. Only one of these three is a fundamental physics parameter. The choices of energy sensitivity and baseline are used to define characteristics of detectors used for measurements of the various mass splitting parameters and oscillation mixing angles.

Note that the oscillation probability is insensitive to the sign of the mass splitting parameter.

2.1.3 Matter Effects in Oscillation

Calculations up to this point have assumed neutrinos oscillating in vacuum. Modifications required for a description of matter effects begin with a modification of the Hamiltonian

with a potential, V , due to coherent forward scattering of neutrino on electrons and nucleons in the medium [43].

$$H = H_0 + V \quad (2.12)$$

The value of H_0 is the value of vacuum Hamiltonian. In the two-flavor case, the Hamiltonian can be shown [40, 44] to be

$$H_0 = \frac{\Delta m^2}{4E} \begin{pmatrix} -2\cos 2\theta & \sin 2\theta \\ \sin 2\theta & 0 \end{pmatrix}. \quad (2.13)$$

where θ is the mixing angle associated with the 2x2 PMNS matrix. If this effect leaves the neutrino momentum unchanged, the resulting additional terms in the Hamiltonian may interfere with the propagation of the unscattered neutrinos. The potential includes contributions from both charged current and neutral current interactions, although the charged current interactions arise solely from the electron neutrinos. The potential, expressed in the flavor basis, is then

$$V_{CC,\alpha} = \begin{cases} \sqrt{2} \pm G_F n_e(x) & \alpha = e \\ 0 & \alpha = \mu, \tau \end{cases} \quad V_{NC,\alpha} = -\frac{G_F}{\sqrt{2}} n_e(x) \quad \alpha = e, \mu, \tau \quad (2.14)$$

where a + is used for neutrinos and a - is used for antineutrinos, n_e is the density of electrons in the medium, and G_F is the Fermi coupling constant. Note that the angle included here is that of the PMNS matrix in two dimensions. A full description of three flavor neutrino oscillation in the presence of a matter potential is beyond the scope of this work. Further information and explicit forms may be found in [40, 44]. The full three-flavor oscillation calculation is used for this thesis using the Prob3++ code [45, 46], which includes an implementation of matter effects. The electron densities are calculated from the Preliminary Reference Earth Model (PREM) [47].

2.2 Experimental Constraints on Neutrino Oscillations

2.3 Solar Neutrinos: A Hint of Multiple Flavors

Early searches for neutrinos focused primarily on the Sun. The first major experiment, proposed by Ray Davis and John Bahcall, was designed to verify that fusion was the primary energy source of the Sun [48, 49]. While the core of the sun is not directly visible to telescopes, neutrinos produced via nuclear fusion could escape the sun relatively unchanged and be observed at Earth.

The Homestake experiment, named for Homestake mine in South Dakota, used 615 tons of perchloroethylene to measure neutrinos via the inverse beta decay reaction



The production rate was well-measured, with a rate of 0.48 counts per day and a background of 0.09 counts per day due to interactions from cosmic ray induced muons [50]. In the typical units of the solar neutrino experiments, this worked out to

$$(\sigma\phi) = 2.56 \pm 0.16 \pm 0.16 \text{ SNU} \quad (2.16)$$

where $1 \text{ SNU} = 10^{-36}$ captures/nucleus/second. The expected rate of neutrino interactions from the sun, however, was predicted to be 8.00 ± 0.97 SNU given the solar models at the time. The Homestake experiment, therefore, was only observing approximately 30% of the predicted interaction rate. New measurements from other experiments, such as SAGE [51], GALLEX [52], and GNO [53] confirmed the results, although with a reduction of around 50% instead of 70% compared to theoretical expectations.

The disagreement between the number of neutrinos expected and the number predicted was not definitively solved until the Sudbury Neutrino Observatory (SNO) experiment. SNO was a detector located 2 km underground in Sudbury mine in Canada [34]. The detector consisted of a large tank filled with heavy water surrounded by photo-multiplier tubes for the detection of Cherenkov emission. By introducing heavy water, SNO was sensitive to not only the charged current interactions of previous experiments, but also to neutral current interactions invisible to the inverse beta decay experiments.

SNO detected the neutral current and charged current interactions via two distinct channels. The charged-current interactions caused a deuterium atom to break down into two separate protons while also transforming the neutrino into an electron. The electron would be produced with an energy high enough to emit Cherenkov radiation and could, therefore, be observed directly, with the energy of the electron used to constrain the incident neutrino spectrum. The primary charged current interaction at SNO was only sensitive to electron flavor neutrino interactions.

The neutral current interactions, with a threshold energy of 2.22 MeV, were able to separate the deuterium in the heavy water, leading to a free neutron in the detector. The detection of the free neutron posed initial challenges for the same fundamental reason that neutrino detection is difficult: neutrons are not charged and therefore do not emit electromagnetic radiation. Instead, early detections of these neutrons relied on the emission of a high energy gamma ray when the neutron was captured on a deuterium atom. The gamma ray could then, in turn, be absorbed on an electron, accelerating the charged particle and producing Cherenkov radiation.

Measurements at SNO were divided between these two measurement channels in order to investigate one possible solution to the missing solar neutrinos: neutrino oscillations [54]. Because the three known neutrino states all have the same neutral current interaction cross section, the neutral current rate is expected to be constant in the presence of oscillations. The charged current rate is, however, expected to change due to the different couplings of each neutrino flavor to the W^\pm boson. Measuring both the neutral current and charged current rates therefore provided a direct test of neutrino oscillations, allowing researchers to identify the effect independent of the solar model.

SNO expected a rate of neutral current interactions from solar neutrinos of $5.05 \times 10^6 \text{ cm}^{-2} \text{ s}^{-1}$ and observed

$$\phi_{NC}(\nu \text{ active}) = 5.25 \pm 0.16(\text{stat})^{+0.11}_{-0.13} \times 10^6 \text{ cm}^{-2} \text{ s}^{-1} \quad (2.17)$$

a result consistent with expectations. The charged current interaction was measured to be

$$\phi_{CC}(\nu_e) = (0.301 \pm 0.033) \phi_{NC}(\nu \text{ active}) \quad (2.18)$$

clearly indicating that the number of electron neutrinos was well below expectations. The combination of these two results gave the first clear indication of neutrino oscillations, a result which earned the SNO collaboration a Nobel Prize in 2015 [55].

2.4 Super-Kamiokande and Atmospheric Neutrinos

While the SNO experiment was working to identify the source of the solar neutrino deficit, the Kamioka Nucleon Decay Experiment (KamiokaNDE) and its successor, Super-Kamiokande (Super-K), were using a similar water Cherenkov detector to search for proton decay. The primary background for this rare process is neutrino interactions. Unlike SNO, however, Super-Kamiokande was sensitive to both MeV solar neutrinos and higher energy GeV neutrinos produced in the atmospheric showers from cosmic ray interactions.

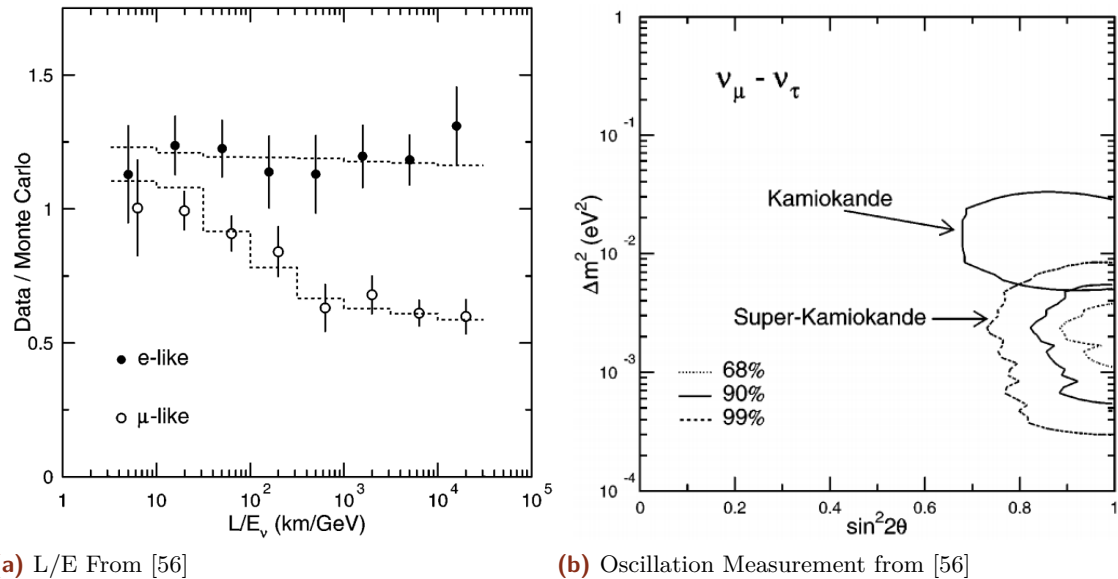


Figure 2.1 – The first atmospheric neutrino oscillation measurements from the Super-K experiment. (a) The ν_e -like events show no shape in L/E, as expected from a lack of neutrino oscillations. The ν_μ -like interactions, however, show a clear drop, indicating the presence of oscillation effects. (b) Using the two neutrino approximation, Super-K produced contours of the best-fit oscillation parameters for $\nu_\mu \rightarrow \nu_\tau$ oscillations. Both figures from [56]

lofsubfigure\newline(a)L/E From [56]lofsubfigure\newline(b)Oscillation
Measurement from [56]

While investigating backgrounds, Super-Kamiokande observed an interesting deficit in the atmospheric neutrino signal. Unlike the case in the solar neutrinos, the deficit observed by Super-K was observed solely in the muon neutrino events with no effect seen in the electron neutrinos [56]. Using the reconstructed energy and direction of events, Super-K was able to show that the number of fully contained events of ν_μ -like interactions changed as a function of L/E - a clear signature of neutrino oscillations in the atmospheric neutrinos. The figure, reproduced in Figure 2.1a, was used, in part, with a 2x2 approximation to the PMNS matrix to produce the first measurements, shown in Figure 2.1b, of the atmospheric oscillation parameters. For the discovery of atmospheric neutrino oscillations at the same time as SNO's discovery of solar neutrino oscillations, the Super-K collaboration was jointly awarded the 2015 Nobel Prize [55].

2.4.1 Global Fits to Oscillations

Since the initial discoveries of SNO and Super-K, many experiments have measured neutrino oscillations. Global fits are performed and updated regularly [57, 58].

The most recent results are shown in Figure 2.2 and include information from solar, reactor, and atmospheric oscillation experiments. The results explicitly assume unitarity and three neutrino species.

	NuFIT 3.2 (2018)			
	Normal Ordering (best fit)		Inverted Ordering ($\Delta\chi^2 = 4.14$)	Any Ordering
	bfp $\pm 1\sigma$	3σ range	bfp $\pm 1\sigma$	3σ range
$\sin^2 \theta_{12}$	$0.307^{+0.013}_{-0.012}$	$0.272 \rightarrow 0.346$	$0.307^{+0.013}_{-0.012}$	$0.272 \rightarrow 0.346$
$\theta_{12}/^\circ$	$33.62^{+0.78}_{-0.76}$	$31.42 \rightarrow 36.05$	$33.62^{+0.78}_{-0.76}$	$31.43 \rightarrow 36.06$
$\sin^2 \theta_{23}$	$0.538^{+0.033}_{-0.069}$	$0.418 \rightarrow 0.613$	$0.554^{+0.023}_{-0.033}$	$0.435 \rightarrow 0.616$
$\theta_{23}/^\circ$	$47.2^{+1.9}_{-3.9}$	$40.3 \rightarrow 51.5$	$48.1^{+1.4}_{-1.9}$	$41.3 \rightarrow 51.7$
$\sin^2 \theta_{13}$	$0.02206^{+0.00075}_{-0.00075}$	$0.01981 \rightarrow 0.02436$	$0.02227^{+0.00074}_{-0.00074}$	$0.02006 \rightarrow 0.02452$
$\theta_{13}/^\circ$	$8.54^{+0.15}_{-0.15}$	$8.09 \rightarrow 8.98$	$8.58^{+0.14}_{-0.14}$	$8.14 \rightarrow 9.01$
$\delta_{CP}/^\circ$	234^{+43}_{-31}	$144 \rightarrow 374$	278^{+26}_{-29}	$192 \rightarrow 354$
$\frac{\Delta m_{21}^2}{10^{-5} \text{ eV}^2}$	$7.40^{+0.21}_{-0.20}$	$6.80 \rightarrow 8.02$	$7.40^{+0.21}_{-0.20}$	$6.80 \rightarrow 8.02$
$\frac{\Delta m_{3\ell}^2}{10^{-3} \text{ eV}^2}$	$+2.494^{+0.033}_{-0.031}$	$+2.399 \rightarrow +2.593$	$-2.465^{+0.032}_{-0.031}$	$-2.562 \rightarrow -2.369$ $\left[+2.399 \rightarrow +2.593 \atop -2.536 \rightarrow -2.395 \right]$

Figure 2.2 – The global best-fit values for the three flavor neutrino oscillation fits as of November 2017. The first column shows results assuming the normal ordering while the second column shows the results for the inverted ordering. Image taken from [58]

2.5 Unitarity and Sterile Neutrinos

While global fits assume three flavors of neutrinos, additional neutrino flavors are theoretically possible. The number of active neutrino flavors is limited to the three known flavors from the measurements of ALEPH (see the discussion of Section 1), although such measurements implicitly only measure the number of species with a coupling to the Z boson [9]. Additional flavors with no or very small couplings to the Z boson may be allowed [59]. New neutrino flavors introduced with these properties are known as *sterile neutrinos*.

2.5.1 Sterile Neutrinos

Models of sterile neutrinos assume that no weak interactions are available to the new species, leaving only interactions with the world via oscillations. In this model, neutrinos oscillate using a 4x4 (or larger NxN) PMNS matrix [40, 60, 61, 59].

$$\begin{pmatrix} \nu_e(x) \\ \nu_\mu(x) \\ \nu_\tau(x) \\ \nu_s(x) \end{pmatrix} = U_{4 \times 4} \begin{pmatrix} \nu_e(x) \\ \nu_\mu(x) \\ \nu_\tau(x) \\ \nu_s(x) \end{pmatrix} = \begin{pmatrix} U_{e1} & U_{e2} & U_{e3} & U_{e4} \\ U_{\mu 1} & U_{\mu 2} & U_{\mu 3} & U_{\tau 4} \\ U_{\tau 1} & U_{\tau 2} & U_{\tau 3} & U_{\tau 4} \\ U_{s1} & U_{s2} & U_{s3} & U_{s4} \end{pmatrix} \begin{pmatrix} \nu_1(x) \\ \nu_2(x) \\ \nu_3(x) \\ \nu_4(x) \end{pmatrix} \quad (2.19)$$

The additional terms in $U_{4 \times 4}$ lead to new mixing angles, θ_{14} , θ_{24} , and θ_{34} . The new terms may be used in the standard oscillation framework introduced in Section 2.1.1 extended with a fourth flavor state, ν_s , and mass state, ν_4 .

$$P(\nu_\alpha \rightarrow \nu_\beta) = \sum_i^4 U_{\beta i}^* U_{\alpha i} \sum_j U_{\beta j} U_{\alpha j}^* e^{i(E_i - E_j)t} \quad \alpha, \beta = e, \mu, \tau, s \quad (2.20)$$

Unlike the three active neutrinos, sterile neutrinos cannot interact with matter, leading to a deficit in the neutrino rates from oscillations of the form $P(\nu_\alpha \rightarrow \nu_s)$. The location and size of the deficit is determined by the oscillation parameters associated with the ν_s and ν_4 states. Sterile neutrinos may be indirectly observed through this deficit by studying the active neutrinos with either charged current or neutral current interactions.

2.5.2 Direct Searches for Steriles

While oscillation of the three active neutrinos preserves the total neutral current rate, sterile neutrinos do not. This provides a unique experimental signature for sterile neutrinos. Dedicated searches for this disappearance have been performed by MINOS [62, 63] and NO ν A [64] with assumptions on the new terms of the mixing matrix. The effect of three sterile hypotheses on the MINOS data is shown in Figure 2.3a. Around 15% of the neutral current events disappear in the three hypotheses tested by MINOS. The results of the NO ν A search are shown in Figure 2.3b.

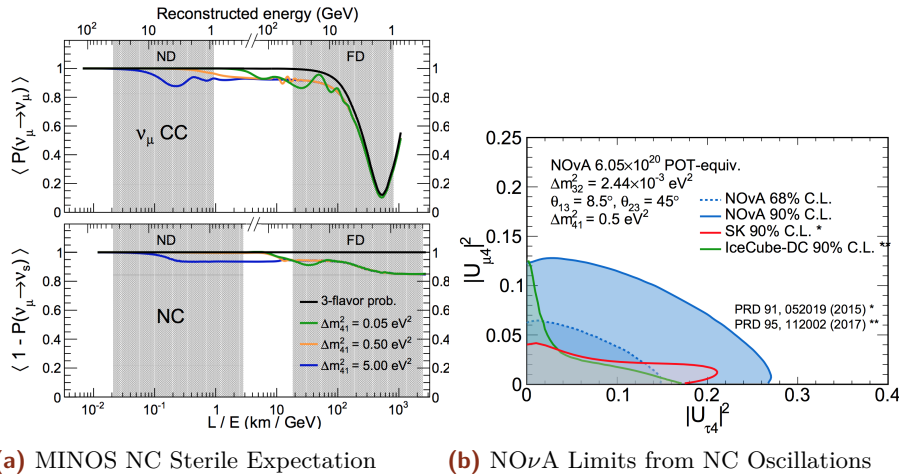


Figure 2.3 – Expectations (a) and results (b) of searches for sterile neutrinos in the neutral current interactions. (a) Effect of three hypothetical sterile neutrinos on the measurements of the MINOS detector [63]. "ND" and "FD" refer to the near and far detector of MINOS respectively. The sterile neutrinos have a small effect on the main oscillation minimum in the charged current channel, but up to 15% of the neutral current events are lost. (b) The results of the NO ν A search for sterile neutrinos using neutral current events. The limits are interpreted in terms of the 4x4 PMNS mixing elements in order to compare to searches with charged current interactions in Super-Kamiokande [65] and IceCube-DC [66].

lofsubfigure\newline\newline(a)MINOS NC Sterile
Expectationlofsubfigure\newline\newline(b)NO ν A Limits from NC Oscillations

Most experiments attempt to investigate one of the additional terms only, assuming the remainder to be negligible [65, 66, 67]. The results rule out large mixing between a hypothetical sterile neutrino and the three active flavors, although small mixing angles are still allowed by experiments [61, 59].

2.5.3 Indirect Searches for Steriles Using Unitarity

Experiments need not search for direct evidence of new mixing terms, however. The addition of a fourth generation of neutrino would have consequences for neutrino oscillation measurements performed in the 3x3 PMNS framework. Standard 3-flavor oscillation measurements may therefore be used to place limits on sterile neutrinos.

The PMNS matrix gives the change in basis and is assumed to be unitary. The unitary condition imposes summation rules for both the rows and columns of the matrix.

$$\sum_i U_{\alpha i} U_{\beta i}^* = \delta_{\alpha\beta} \quad \alpha, \beta = e, \mu, \tau \quad (2.21)$$

$$\sum_i U_{\alpha i} U_{\alpha j}^* = \delta_{ij} \quad i, j = 1, 2, 3 \quad (2.22)$$

If the neutrino mixing matrix consists of more than the three known active neutrinos, however, these unitary relations would only hold in higher dimensions. When projected down to the observed 3x3 PMNS matrix, non-unitarity would be observed.

Neutrino oscillation measurements are performed with the assumption of 3x3 unitarity imposed, allowing the PMNS matrix to be rewritten in terms of three mixing angles and a single phase. The appearance and disappearance probabilities in oscillation measurements are typically written in terms of these mixing angles. Using these mixing angles, the disappearance probability for atmospheric oscillations of $\nu_\mu \rightarrow \nu_\tau$ is given by

$$\begin{aligned} P(\nu_\mu \rightarrow \nu_\mu) &= 1 - \left| \sum_i U_{\mu i}^* U_{\mu i} e^{-im_i^2 L/2E} \right|^2 \\ &= 1 - \left(\cos^2 \theta_{13} \sin^2 2\theta_{23} + \sin^4 \theta_{23} \sin^2 2\theta_{13} \right) \sin^2 \left(\frac{\Delta m_{31}^2 L}{4E} \right) \\ &\approx 1 - \sin^2 2\theta_{23} \sin^2 \left(\frac{\Delta m_{31}^2 L}{4E} \right). \end{aligned} \quad (2.23)$$

where the final approximation has been made due to the small value of θ_{13} . The atmospheric appearance probability, $\nu_\mu \rightarrow \nu_\mu$, is given by

$$\begin{aligned} P(\nu_\mu \rightarrow \nu_\tau) &= \left| \sum_i U_{\mu i}^* U_{\tau i} e^{-im_i^2 L/2E} \right|^2 \\ &= \left(\cos^2 \theta_{13} \sin^2 2\theta_{23} \right) \sin^2 \left(\frac{\Delta m_{31}^2 L}{4E} \right) \\ &\approx \sin^2 2\theta_{23} \sin^2 \left(\frac{\Delta m_{31}^2 L}{4E} \right). \end{aligned} \quad (2.24)$$

The form of the oscillation probabilities for appearance and disappearance are very similar when written in terms of the mixing angles. However, the appearance and appearance probabilities in neutrino oscillation measurements depend on different elements of PMNS mixing matrix. Because of the difference in the elements probed, appearance and disappearance measurements may be interpreted to give limits on the fundamental elements of the mixing matrix without imposing unitary.

This method of searching for sterile neutrinos may be applied to global fits, reinterpreting standard oscillation measurements to place limits on the size of any non-unitarity. Using the unitarity conditions of Equation 2.21 and 2.22, limits on the size of non-unitarity have been calculated[68]. Experimental constraints from a number of experiments (see reference 26 of [68]) were used to evaluate the best-fit mixing matrix. The unitarity constraints were tested by looking at the potential deviation of each row or column

$$\Delta U_\alpha = 1 - \left(|U_{\alpha 1}|^2 + |U_{\alpha 2}|^2 + |U_{\alpha 3}|^2 \right) \quad \alpha = e, \mu, \tau \quad (2.25)$$

or

$$\Delta U_i = 1 - \left(|U_{\alpha i}|^2 + |U_{\beta i}|^2 + |U_{\delta i}|^2 \right) \quad i = 1, 2, 3 \quad (2.26)$$

The results are shown in 2.4. The constraints on unitarity of the 3x3 mixing matrix are strongest in the muon and electron sector, with constraints nearly an order of magnitude stronger than that observed in the tau sector. This is a result of limited measurements directly involving ν_τ oscillations.

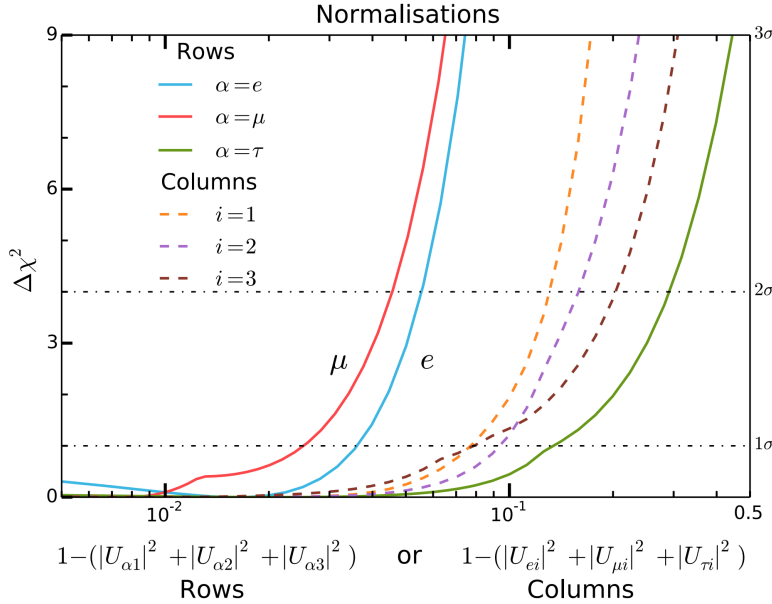


Figure 2.4 – The results of the tests using 2.25 (solid) and 2.26 (dotted). A smaller value on the x-axis indicates a tighter constraint on observed unitarity of the 3x3 mixing matrix. Tests involving only muon or electron flavors show significantly tighter constraints than those including the tau flavor. Image taken from [68]

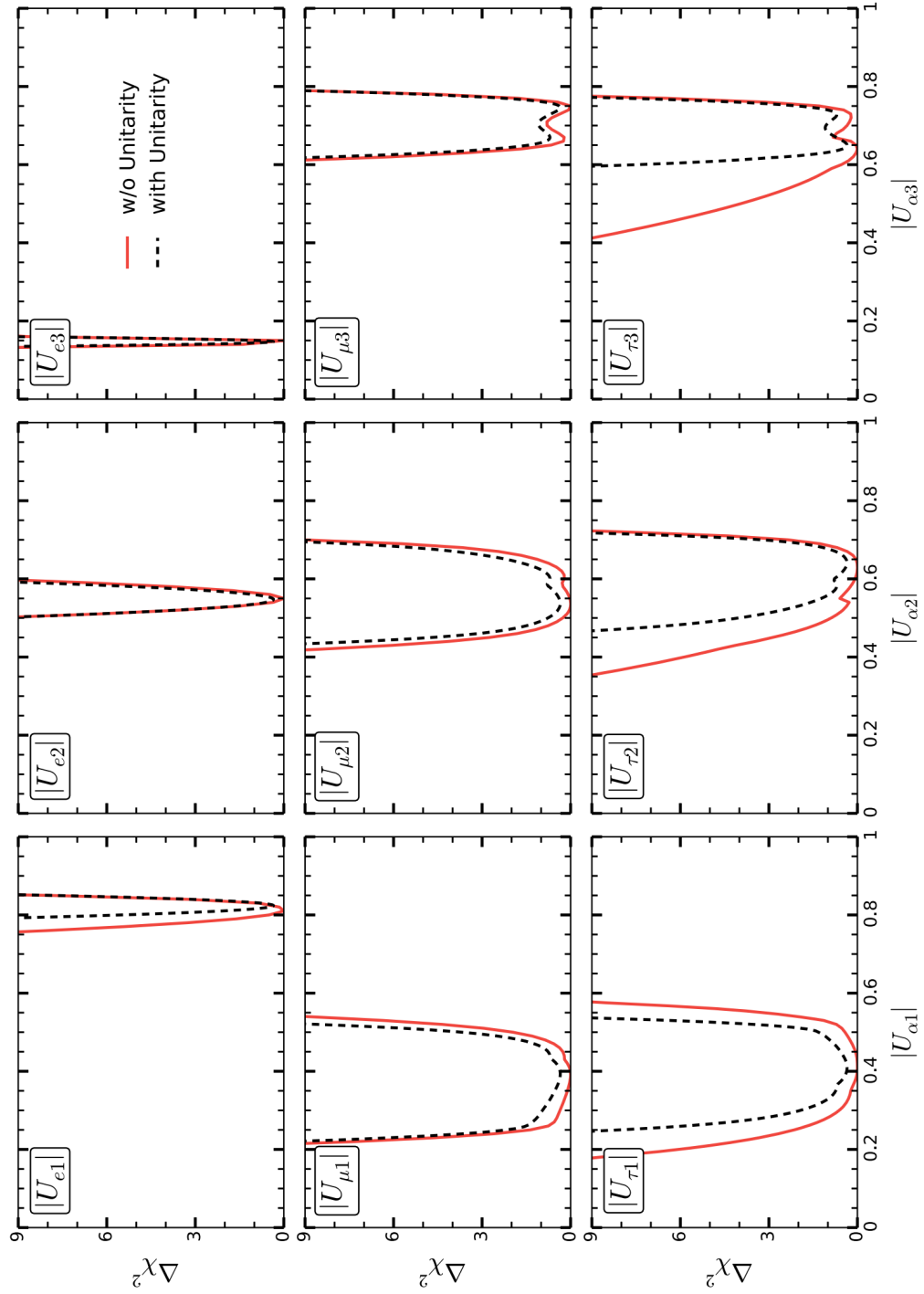


Figure 2.5 – The constraints from a global fit to neutrino oscillation data[68] with an assumption of unitarity (black dotted) or no assumption of unitarity (red solid). The first two rows show little change from the unitarity assumption, indicating strong constraints from direct measurements. The elements of the third row, related to the ν_τ , show much larger changes, indicating that constraints are obtained from indirect oscillation measurements.

When the individual limits for each element of the 3x3 PMNS matrix are checked, it is the tau sector that shows the largest uncertainties. Measurements of ν_τ oscillations therefore can provide valuable information on unitarity in the neutrino sector, leading to indirect constraints on sterile neutrino hypotheses.

The IceCube Detector

The low cross section of neutrinos is a challenge for experimentalists. There exist two avenues for the measurement of neutrinos. The precise measurements of individual events, used most notably in the OPERA [22] and DONUT [7] to identify individual events, gives unique constraining power with low backgrounds. More common, however, is the use of large experimental volumes to collect high-statistics neutrino samples. For the study of atmospheric neutrinos, volumes on the order of a kiloton are required.

The IceCube Neutrino Observatory is currently the largest neutrino detector in the world, encompassing a volume of 1 km^3 of glacial ice at the geographic south pole. The design of the IceCube detector is also presented in this chapter, beginning with a description of the DOMs that make up the primary detectors within the IceCube observatory (Section 3). The overall geometry of the detector is discussed in Section 3.1.6 with a focus on the differences between the larger IceCube detector and the DeepCore subarray used for oscillation searches.

3.1 The DOM: The Basic Unit of IceCube

3.1.1 The Photomultiplier Tube

The basic unit of the IceCube detector is the *digital optical module*, often referred to simply as the *DOM* [37]. The DOM is designed around a downward-facing 10 inch R7081-02 photomultiplier tube (*PMT*) from Hamamatsu Photonics [69, 70] and includes onboard electronics for standard operation as shown in Figure 3.1. Circuit boards are included for data acquisition, control, calibration, communications and power conversion as well as for high voltage input from the surface. The electronics of the DOM are encased in a spherical glass housing designed to withstand the high pressures associated with operation in the glacier of Antarctica. The PMT is optically coupled to the glass housing in order to minimize distortion of incoming light.

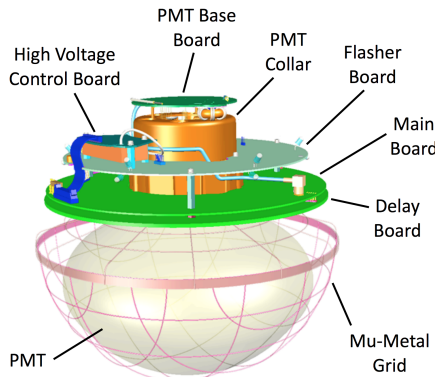


Figure 3.1 – The IceCube DOM contains multiple components, including the PMT itself as well as various electronics necessary for semi-autonomous operation.

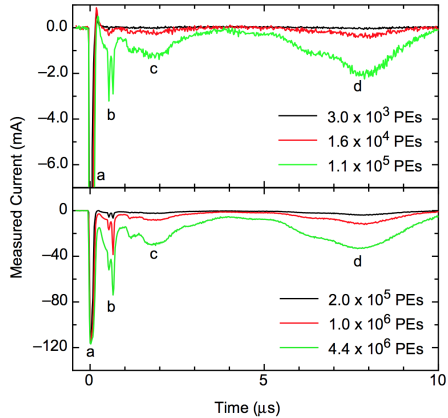


Figure 3.2 – Afterpulsing calibration measurements performed in the lab. LEDs with known brightness were flashed to test for offtime response of the IceCube PMT. Clear dips, corresponding to detected charge, are visible. Drop (a) corresponds to the initial LED flash while (b), (c), and (d) show prominent afterpulsing peaks. Image taken from [69].

Pre-, Late-, and Afterpulsing

Measurement with the IceCube photomultiplier tubes introduces known effects in the recorded charge. These effects are divided into *pre-pulses*, *late-pulses*, and *afterpulses*. The pre-pulses, arriving within a few dozens of nanoseconds prior to the main signal, are thought to arise from the small probability of an electron bypassing one of the dynodes. Late-pulses are likewise thought to be produced by electrons which return to a previous dynode, inducing a signal a few dozens of nanoseconds immediately following the main signal. These signals tend to be small and inconsequential for physics measurements. After-pulses, which arise from ionization of residual gases in the PMT, are a more significant concern for calibration work as addressed in Section 5.1. The ionized atoms tend to travel significantly more slowly than electrons, resulting in a delay between the main signal and the subsequent afterpulses that may be as large as 10 microseconds.

3.1.2 The Discriminator Used for DOM Triggering

A discriminator onboard the DOM is used to identify signals from the PMT with a voltage threshold corresponding to 0.25 photoelectrons (*PE*). Each discriminator crossing begins a *DOM launch*, the lowest level signal available in the IceCube detector containing a representation of the raw PMT output in the form of a *waveform*. Launches are stored in DOM memory while awaiting a decision from the triggering system.

3.1.3 Local Coincidence

If any of the notified DOMs also record a launch within a configurable 1 microsecond window, both launches are said to form a *hard local coincidence (HLC)* pair. Nearby DOMs, here defined to be either of the two DOMs above or below the current DOM, are notified of the launch via a signal sent using the *local coincidence* wiring. Launches which fail to satisfy the local coincidence conditions are referred to as *soft local coincidence (SLC)* hits. Launches recorded as part of an HLC pair receive a flag. This flag may be used to later identify only those launches which satisfy the local coincident conditions, providing a simple, default method of identifying hits likely to be caused by particle interactions in the detector.

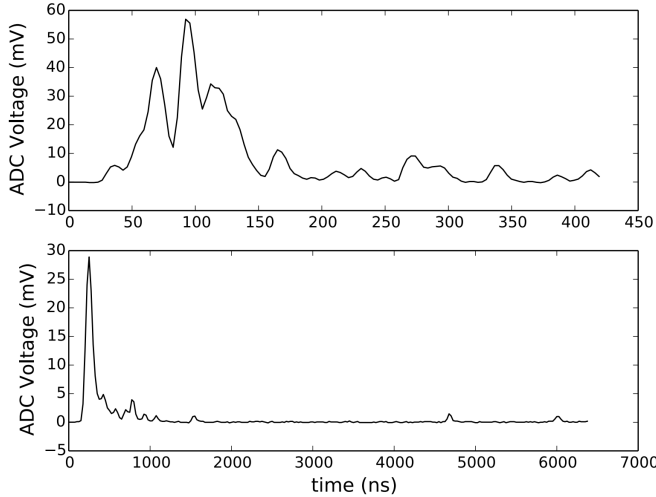


Figure 3.3 – Examples of the ATWD (top) and FADC (bottom) waveforms output from an IceCube PMT. Taken from [37]

3.1.4 Digitization

While awaiting a local coincidence decision, the waveform of a launching DOM is passed to the two onboard digitizers. Information from the PMT is digitized using the fast analog-to-digital converter (*fADC*), which provides binned information at 40×10^6 samples/second for the 6.4 microseconds following the initial DOM launch [37]. Simultaneously, the *Analog to Digital Waveform Digitizer*, or *ATWD*, will digitize the waveform using 322 bins with 3.3 nanoseconds per bin.

If a launch satisfies the HLC conditions, the DOM will request the full digitization of the waveforms from both the ATWD and FADC, providing a complete record of the launch. Examples of digitized waveforms from the ATWD and fADC are shown in Figure 3.3.

When digitizing a signal, the ATWD experiences up to 29 microseconds of deadtime [37]. During this time, the secondary ATWD is available to record further pulses, resulting in a total average fractional deadtime per DOM of 2.2×10^{-5} seconds/second. In addition, each of the two ATWDs possesses three channels with separate gains. This provides the ability to accurately measure the waveform, even in cases of saturation. The unsaturated ATWD with the highest gain provides a record for the launch.

If the launch is instead given the SLC label, the information in the ATWD is lost and the FADC instead digitizes only the three bins associated with the largest peak of the waveform. While this limits the information available for these launches, the lack of associated nearby launching DOMs provides strong evidence that the launch is due to random detector noise.

3.1.5 Noise in IceCube DOMS

Dedicated measurements using IceCube DOMs have shown multiple components to the detector noise[71]. A large fraction of the detector noise displays non-Poissonian behavior in time [37]. The model used in IceCube, shown in Figure 3.4, splits the detector noise into *Poissonian* and *non-Poissonian(time-correlated)* noise.

The Poissonian noise consists of thermal noise and radioactive decays in the glass of the PMT and DOM. Studies of these radioactive components are ongoing, with some evidence that Potassium-40 and Uranium-238 may be responsible for at least some of the observed decays. Once a decay occurs, a rapid series of pulses occurs in the PMT,

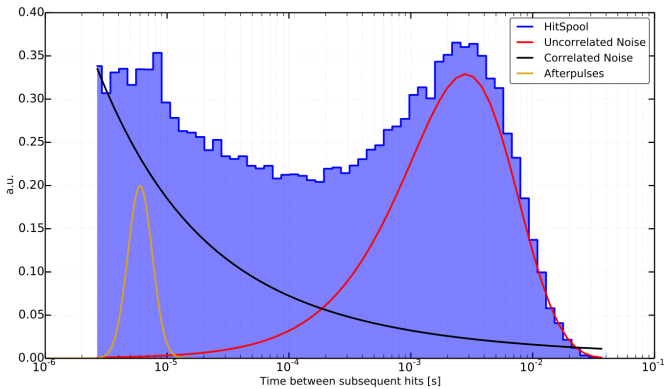


Figure 3.4 – A histogram of the time between subsequent hits on DOM 15 of string 27. HitSpool data, specialized data collected with no trigger applied, is shown in blue. The "correlated" (non-Poissonian) and "uncorrelated" (Poissonian) features are shown in red and black respectively. The location of a large afterpulsing peak is shown in yellow. Note that the features included are not to scale. Image taken from [37].

leading to a "burst" of noise that continues for up to a few milliseconds [71]. These hits are believed to be due to a scintillation or luminescence process.

The typical averaged noise rate is 560 Hz for standard IceCube DOMs and 780 Hz for high quantum efficiency DOMs. Poissonian noise makes up approximately 250 Hz of this rate with the remainder due to non-Poissonian processes.

3.1.6 Triggering in IceCube

Digitized versions of the waveforms are transmitted from the DOM to the IceCube physics data acquisition system (*pDAQ*) for use in trigger and event building. The most common type of trigger used in IceCube analyses is the *Simple Majority Trigger* or *SMT*. This trigger is designed to look for coincidences between DOMs using HLC launches. Each of the SMTs is defined by three fundamental configurations: a DOMSet, which lists the DOMs available for use in the trigger conditions; a threshold number of HLC launches before the trigger fires; and a time window length in which the HLC are required to coexist.

Once all triggers are identified, a *global trigger* is defined. This consists of the superset of all triggers occurring within 10 microseconds of one another. All detector readout enclosed within the global trigger as well as additional information within an additional 10 microseconds both before and after the trigger is combined into a single *event*.

3.2 The Geometry of the Detector

The IceCube detector is located at the geographic south pole in Antarctica. The Antarctic glacier forms a 3 km deep surface of clear ice over the bedrock. IceCube uses the Antarctic glacier as both a support structure and as a detection medium for Cherenkov radiation. The IceCube observatory consists of three distinct subarrays, shown in Figure 3.6, each optimized for separate physics measurements. A total of 5160 DOMs make up the IceCube in-ice array with an additional 324 DOMs used at the surface in the IceTop air shower array [37]. IceCube DOMs are deployed at depths between 1450 m and 2450 m below the surface to shield the detector from atmospheric background muons. The DOMs are deployed in a hexagonal grid in a series of 86 *strings*, each of which provides connections and support for 60 DOMs. Strings are spaced approximately 125 m apart

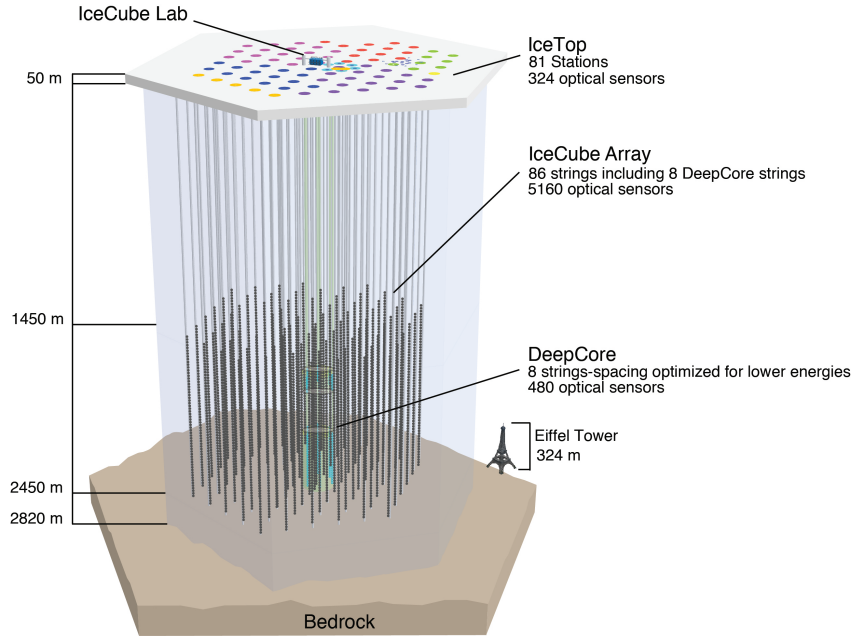


Figure 3.5 – The IceCube Neutrino Observatory. Three separate subdetectors are shown: IceTop, a cosmic ray air shower detector; IceCube, an array designed to search for astrophysical neutrinos; and DeepCore, a dense subarray optimized for atmospheric oscillation physics measurements. The detector was deployed over multiple years. Strings deployed in the same year are shown with identical colors at the surface.

with DOMs space 17 m apart on each string. Each DOM in the IceCube detector is assigned a unique string number (1-86) and DOM number (1-60).

Additional strings were installed in the glacier annually from 2004 until 2010 with partial detector data collected during construction. During the final years of construction, a denser section of the detector was built, known as DeepCore [72]. The DeepCore subarray consists of 8 strings equipped with high quantum efficiency PMTs 35% more sensitive than the standard IceCube DOM [69]. The DeepCore strings are split between a *fiducial* volume, in which 50 DOMs are spaced 7 m apart on a string, and a *veto plug* of 10 DOMs 10 m apart as shown in Figure 3.6. The DOMs in the DeepCore fiducial volume are located in the clearest ice of the detector at depths between 2100 m and 2450 m below the surface [73]. The veto cap, installed between 1750 and 1850 m below the surface, is used to identify background muons for DeepCore.

3.2.1 IceCube: A Detector for TeV Neutrinos

The IceCube detector is a regularly spaced hexagonal grid buried in the glacier with the proposed purpose of measuring astrophysical neutrino candidate events and identify the source of cosmic rays. The IceCube array has an energy threshold of around 50-100 GeV with an optimal response above 1 TeV[72, 37].

In the standard IceCube detector, an SMT using all DOMs with a threshold of 8 HLC launches within 5 microseconds is typically used [37]. This trigger, known as *SMT8* after the number of required hits, is designed for high signal efficiency at energies above 100 GeV with a minimum number of accidental triggers due to random detector noise. The IceCube detector records an SMT8 rate of around 2100 Hz with less than 1 Hz expected from neutrino interactions.

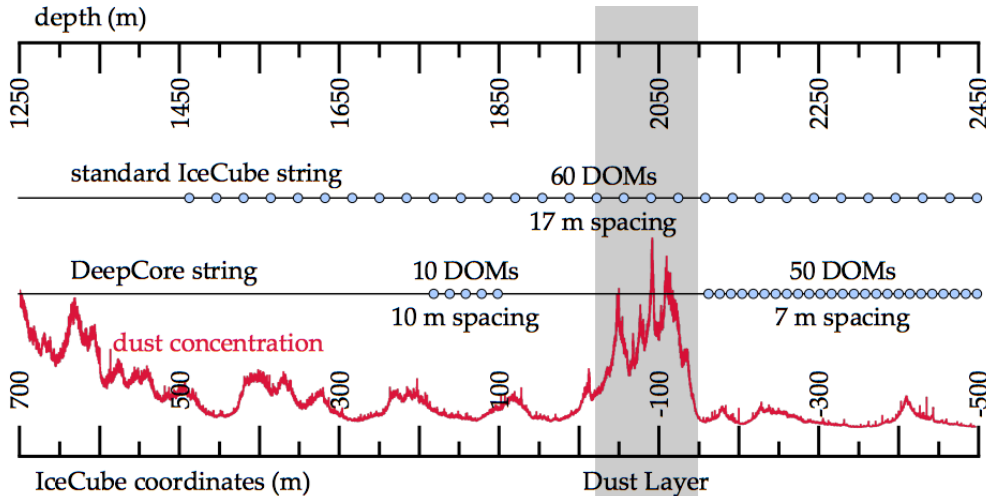


Figure 3.6 – A comparison of the standard IceCube string (right) to the DeepCore string (left). The IceCube string uses DOMs spaced 17 m apart while DeepCore divides the DOMs into a fiducial (bottom) and veto plug (top). The dust concentration is shown in red. The concentration of dust in the ice affects the scattering and absorption of the glacial ice.

Events at the TeV scales of the IceCube detector show well-defined topologies, as shown in Figure 3.7. The IceCube detector has performed many measurements, including searches for sterile neutrinos [67], anisotropy in the cosmic ray flux [74], measurements of the neutrino cross section at high energies [75], and the first discoveries of an astrophysical neutrino flux [76].

3.2.2 DeepCore: Extending the Reach to GeV Scales

The DeepCore detector was designed to be a smaller, denser detector optimized for the measurement of atmospheric neutrino oscillations. The denser spacing and clear ice of DeepCore lower the energy threshold to around 10 GeV [72], permitting the study of oscillations. DeepCore was installed at the bottom of the IceCube array near the center of the IceCube hexagonal grid.

In DeepCore, the desire for lower energy events led to the introduction of a separate trigger, known as *SMT3*. This trigger, using only DOMs within the DeepCore fiducial volume, searches for at least three HLC launches occurring within 2.5 microseconds. This effectively lowers the triggering threshold from roughly 100 GeV with the larger IceCube array to approximately 10 GeV. The SMT3 rate, at 250 Hz [37, 72], is substantially smaller than the SMT8 rate due to both the increased overburden as well as the smaller number of PMTs included in the SMT3 DOMSet. By placing the detector inside of the larger IceCube array, DeepCore allows analyzers to use the IceCube detector as an active veto, reducing the background rate to 17 Hz.

DeepCore events do not show the clean topological separation of the higher energy IceCube events as seen in Figure 3.7. Events may be separated broadly into *cascade-like* and *track-like* statistically using information contained in the timing of hits in the detector. Such separation techniques are energy-dependent and do not perform well at very low energies.

DeepCore has observed atmospheric neutrino oscillations in the $\nu_\mu \rightarrow \nu_\tau$ in the disappearance channel [79, 80, 81], with the most recent measurement showing competitive precision to dedicated measurements performed with particle accelerators.

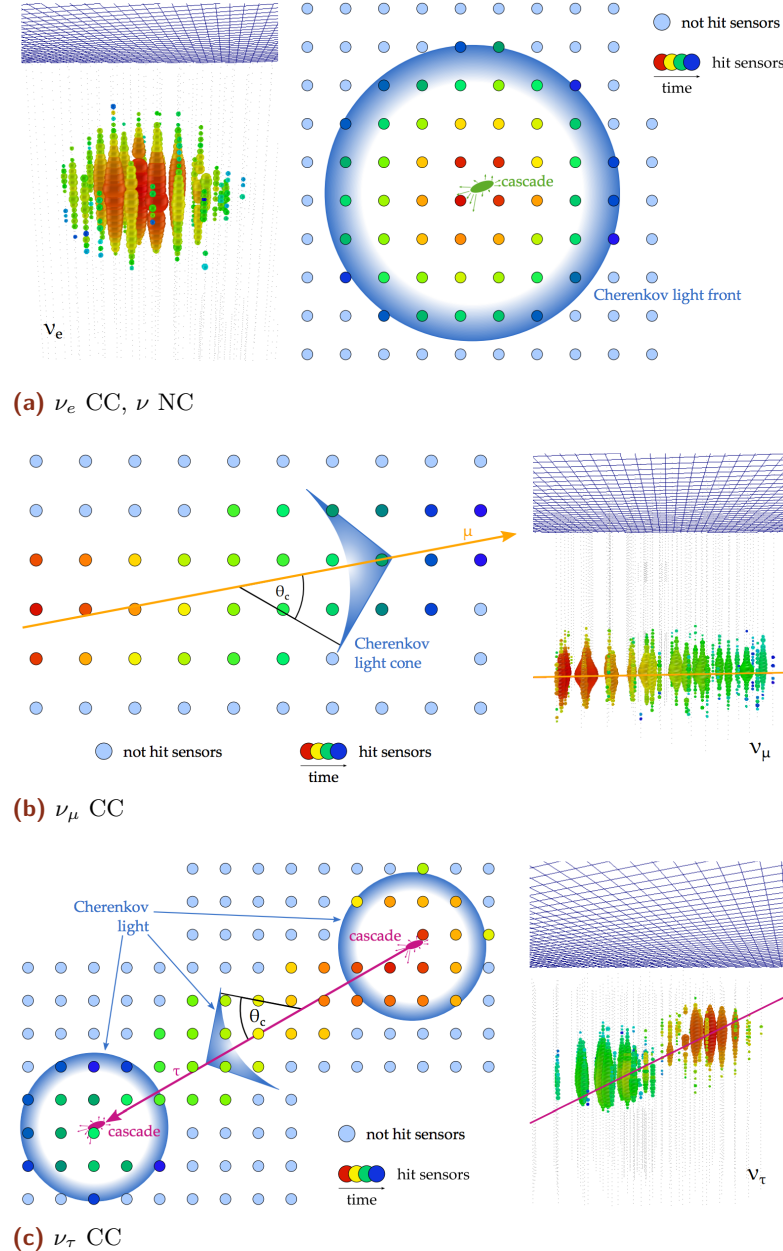


Figure 3.7 – Examples of event topologies above 1 TeV using the full IceCube array. Event views shown in (a) and (b) are from actual events discovered by the IceCube detector [77]. Images taken from [78]. (a) ν_e CC and ν NC show similar behavior from electromagnetic and hadronic interactions, which result in a shower of particles that quickly scatter in the ice. Cherenkov emission from these events appears roughly spherical in the detector. These events are known as "cascades". (b) ν_μ CC events begin with a hadronic interaction, then produce Cherenkov light from the outgoing muon. Above 1 TeV, the track of the outgoing muon becomes clearly visible. (c) Above 10 TeV, the tau lepton from a ν_τ CC may travel a significant distance before decaying. This results in two well-separated cascades in the detector, a tell-tale signature of ν_τ CC interactions.

lofsubfigure\newline(a)\newline(a) ν_e CC, ν NC\nlofsubfigure\newline(b)\newline(b) ν_μ \newline(CC\nlofsubfigure\newline(c)\newline(c) ν_τ CC

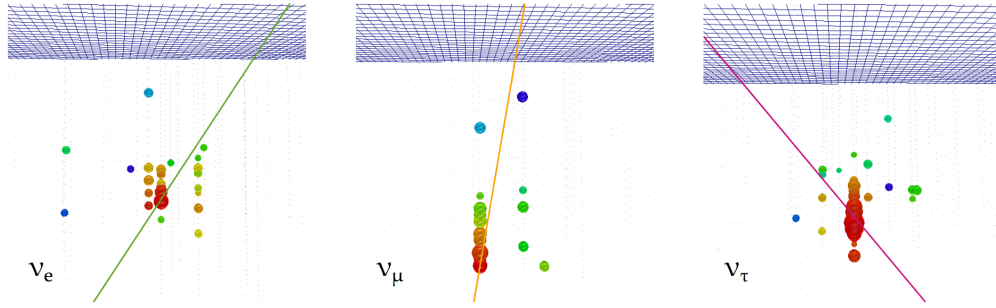


Figure 3.8 – A selection of 50 GeV simulated events in DeepCore taken from [78]. Unlike the event topologies at high energies, DeepCore events do not show distinct event types.

While DeepCore was designed for oscillation physics, the neutrinos may be used for other purposes as well. Recent work with DeepCore has shown sensitivity to studying dark matter interactions in the sun [82] and in the galaxy [83].

3.3 Optical Properties of the Antarctic Glacier

3.3.1 The Bulk Ice Model

The Antarctic glacier, with a thickness of 2.8 km at the geographic south pole [73], forms both the support structure and the interaction medium for IceCube. During deployment, measurements of the scattering properties of the ice were taken during deployment of the IceCube strings. The IceCube dust logger emitted laser light aimed into the undrilled ice and detected backscattered photons[84, 85]. The results are shown in Figure 3.9

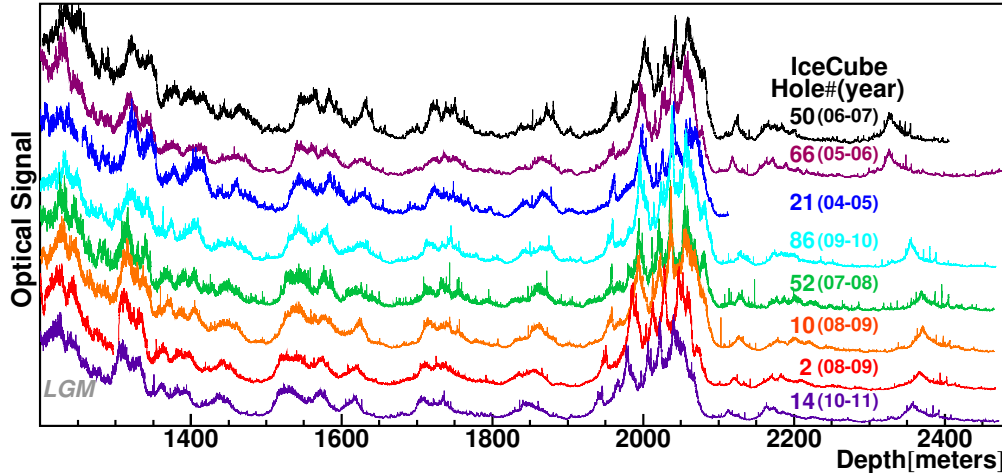


Figure 3.9 – The data from the dust loggers deployed in various drill holes in IceCube during deployment. Data from individual holes has been offset in the y direction for clarity. Larger relative values of the "Optical Signal" represent more scattering in the ice while smaller values indicate clearer ice. The "dust layer" is visible in all drill holes around 2000 m. Deepcore DOMs are deployed below this layer. Image taken from [86].

Peaks are present in the dust logger data due to volcanic events in the Earth's past [84]. The most significant peak, a set of features around a depth of 2000 m, form what is known as the *dust layer* of IceCube, a region with significantly higher scattering and absorption properties than the surrounding ice.

To improve the modeling of the glacier, dedicated measurements have been performed using light-emitting diodes (LEDs, also known as *flashers* in IceCube) onboard the DOMs [73, 37]. In specialized calibration runs, the LEDs are flashed at a few Hertz for a few minutes while nearby DOMs receive the emitted light. Monte Carlo simulations of the flashers are used with varying ice properties in order to identify the most likely properties of the ice. Each flashing and detecting DOM pair provides a set of known times, positions, and light output in the ice, allowing for the properties of the intervening medium to be determined.

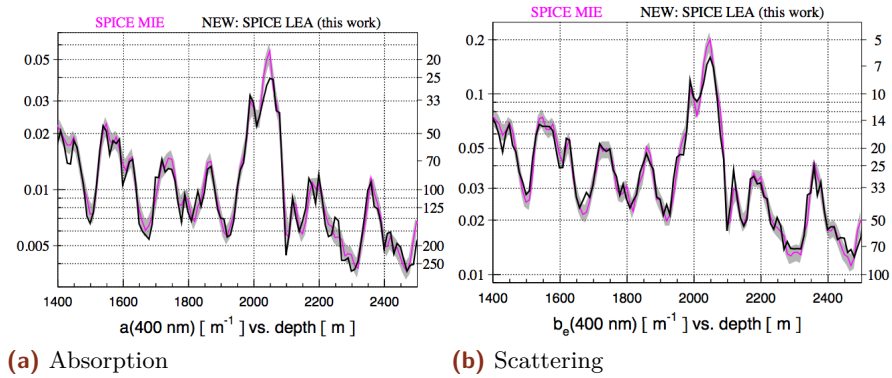


Figure 3.10 – The absorption and effective scattering properties of the ice as fit to flasher data. Two models are shown representing different generations of ice models used for simulation. The "Mie" model does not include anisotropy while the "Lea" model does. Figure from [87].

lofsubfigure\subfigure(a)Absorptionlofsubfigure\subfigure(b)Scattering

The modern ice model used for this thesis consists of three main properties: the absorption, the scattering, and the anisotropy of the ice [87]. The measured properties of the absorption and scattering may be seen in Figure 3.10 while the effect of the anisotropy can be seen in Figure 3.11. Scattering photons change direction, losing information about the direction of the emission source. Absorbed photons are not visible to the detector, potentially modifying the observed number of photons and the reconstructed energy of an event. The anisotropy, consisting of a direction and magnitude, modifies the ice properties as a function of direction due to movement and compression of the glacier over time. The anisotropy affects both the scattering and absorption from each direction in the x-y plane and can affect the azimuthal directions of reconstructions in IceCube.

3.3.2 The Hole Ice

After the strings were deployed, each drill hole was allowed to refreeze. The refrozen column of ice around each string is referred to as the *hole ice*. Using a dedicated camera deployed at the bottom of string 80, the refreezing process of the hole ice has been observed over the course of several years [88, 37]. Images obtained from the camera show the refrozen ice divided into three distinct regions.

The outermost region, the *bulk ice*, is the original glacial ice and is unaffected by the deployment of the detector. The outer part of the drill hole shows improved clarity compared to the bulk ice. The central region of the drill hole, a central core of about 16 cm in diameter, shows significantly worse scattering properties than the bulk ice [37]. This central column, referred to as the *bubble column*, affects the photon acceptance of the PMT. Measurements to characterize the hole ice are ongoing.

find good quality
swedish camera pics?

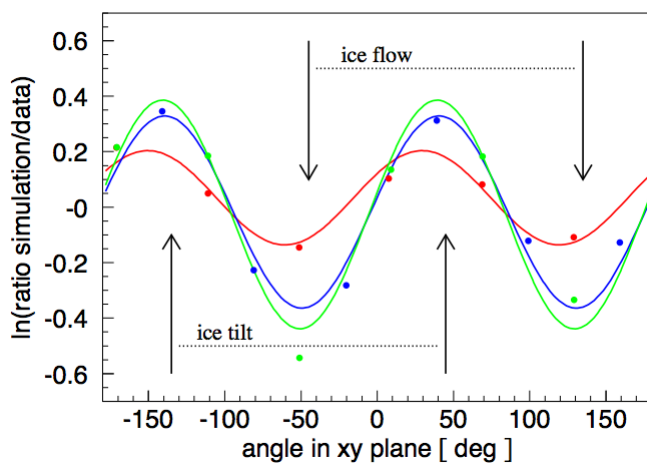


Figure 3.11 – The effect of the anisotropy on the light output from a flasher on string 63. Measurements (points) are shown for receiving DOMs at three distances: at 125 m (red), at 217 m (blue), and at 250 m (green). A line is included to show the expected effect of anisotropy at each distance. The y-axis shows the ratio of a simulation of the same flasher without including anisotropy to data. A modulation is observed as a function of direction in the x-y plane.

Simulation of the IceCube-DeepCore Detector

In order to model both signal and background, *Monte Carlo simulations* of the detector are necessary. In the search for tau neutrinos, this is particularly important due to the low rates and high backgrounds expected, requiring multiple types of simulation for both signal and background.

Simulation in IceCube is broken into three broad stages, each of which will be discussed in turn. The generators used in the appearance analysis are discussed in Section 4. The propagation of the charged leptons and photons are then described in Section 4.2. Section 4.2.3 describes the simulation of the detector, including the PMT electronics and the detector noise.

4.1 Monte Carlo Generators

4.1.1 Background Generation

CORSIKA

The primary background for the observation of atmospheric neutrino events is the other particles present in the cosmic ray interactions in the atmosphere. These interactions produce many particles, most of which are stopped before reaching IceCube by the shielding provided by the Antarctic Glacier. In order to correctly account for the interactions and decays of these particles, the *CORSIKA* generator from Karlsruhe Institute of Technology is used[89]. The CORSIKA generator is a collection of code designed to simulate, interact, and propagate a cosmic ray air shower from the interaction point in the upper atmosphere to the surface. Originally designed for use with surface detectors such as Auger, HAWC, and IceTop, the code has been adapted for use in the IceCube collaboration by identifying the muon (and, sometimes, neutrino) components of the air shower.

CORSIKA has many modes of operation and options for configuration. The standard IceCube simulation of air showers uses the SIBYLL 2.1 hadronization mode [90] to follow the interactions through the shower.

IceCube simulation of air showers uses two possible modes of CORSIKA. The "Polygonato" mode, which generates cosmic rays following the model from [91]. The Polygonato flux parametrized the energy spectra of individual elements of the cosmic ray flux as power laws extrapolated to high energies. In typical IceCube simulation, CORSIKA simulation produced using the Polygonato model includes a mixture of muons from all seasons, effectively producing an averaged flux useful under the assumption of equal livetime throughout the year. The elemental ratios of the generated events follow the Polygonato flux directly, producing a "natural" flux of simulated events [89]. The natural spectrum of the Polygonato CORSIKA simulation has the benefit of allowing a direct physical interpretation of the resulting spectrum without the need for reweighting and simplifies the production of coincident showers, which require a natural spectrum.

The second model, the five-component mode, reduces the full spectrum of cosmic rays to five effective families: hydrogen, helium, nickel, aluminum, and iron. Each of these components is allowed to have different spectral properties. The five-component mode is

useful due to the ease with which the user can modify and reweight to different primary spectra, allowing the investigation of different cosmic ray compositions without the production of dedicated simulation. The simplicity associated with the reweighting of five-component simulation allows IceCube to produce unphysical spectra in order to optimize the production of simulated events necessary for the various analyses. The five-component simulation may be reweighted to match cosmic ray models, including both the Polygonato model and the newer H3a model, which models the cosmic ray flux using three distinct populations of sources [92]. While this slightly complicates the use of the simulation in analyses, the ability to test with various spectra has been an invaluable tool for high energy analyses, which can be sensitive to changes in the cosmic ray spectrum above the knee. Five-component CORSIKA simulation, due to the unphysical generation spectrum, cannot easily be used in the production of simulation involving timing coincidences between events and are currently supplemented by the Polygonato CORSIKA for this purpose.

In both cases, the particles from the air shower are only propagated to the surface of the ice. For analyses using the in-ice array, we take the muons reaching the surface from a CORSIKA simulation and propagate them through the ice, simulating the continuous and stochastic energy losses along the way. The muons are propagated to a surface in the ice consisting of a cylinder with radius 800 meters and length 1600 m centered on the IceCube detector. In order to reach the detector, a muon must result from a cosmic ray interaction of approximately 600 GeV due to the shielding of the glacier. Because of this, CORSIKA simulations typically have a lower energy cutoff of about this value to avoid simulating events that will not reach the detector.

In principle, neutrinos may also be produced using the CORSIKA generator. In practice, this tends to be extremely inefficient for most searches that are no explicitly looking for muons and neutrinos from the same air showers given the extremely low cross section of the neutrino relative to the muon. For this reason, the background generation with CORSIKA in IceCube typically refers to muon events only, with no accompanying neutrino.

MuonGun

CORSIKA simulations are computationally costly and offer few ways to directly control the spectrum of events at the detector. The characteristics of muons produced in an air shower are not known a priori. Targeted simulations in which particular muon samples are required cannot easily be generated with CORSIKA. In situations where the required muon simulation falls within a relatively narrow phase space, whether that be in energy, angle, or position inside of the detector, it can be beneficial to tailor simulation to the needs of specific analyses. Alternatively, there are situations in which the details of the cosmic ray interactions are an unnecessary complication to the final level IceCube analyses. In these situations, IceCube has developed a tool to bypass the full air shower simulation provided by CORSIKA, producing muons directly at a cylindrical surface inside the ice [93]. This tool, known as *MuonGun*, has the benefit of removing the computationally costly simulation of the full air shower, giving the user more control over the resulting simulated events at the cost of information about the initial cosmic ray interactions. This allows targeted, high statistics background simulation samples to be produced for analyses.

In this generator, the muons are produced on a *generation cylinder* with a radius of 800 meters and length of 1600 meters, matching the final muon positions of the CORSIKA

generator. The muons are pulled from a power law spectrum of the user's choice: in this work, an power law is selected with a soft spectral index of -5, an offset of 700 GeV, and a range of 160 GeV to 100 TeV. The lower energy range is selected by using CORSIKA simulation to identify the minimum energy required for a muon at this surface to reach and trigger the DeepCore detector.

The angular spectrum of the MuonGun simulation is created by setting a *target cylinder* toward which the generated muon must intersect. For this work, the DeepCore fiducial volume is used as a target, encompassing a cylinder with radius 150 meters and length 500 meters centered on DeepCore at $x=(46.3, -34.9, -300)$.

These features of MuonGun give the generator significant flexibility, allowing for a very focused simulation of muons that would not otherwise be possible with the current implementation of the CORSIKA generator. The downside, as with all targeted generation, is of course that one must be aware of the limitations. For example, the settings described above will provide a good description of muons reaching and triggering the DeepCore array, but will not include the correct contributions of muons in the outer IceCube detector. This can result in disagreement between data and simulation if the limitations are not acknowledged and accounted for.

This abstraction disassociates the muon at the detector from the air shower, and therefore the cosmic ray, that produced it. In order to properly account for the dependence on the cosmic ray spectrum in the muon weights, dedicated simulations must be produced using the full CORSIKA generator. By following the interaction, showering, and propagation to the detector, IceCube is able to produce an effective parametrization of the association between a particular cosmic ray spectrum and the muons reaching the detector. This must only be done once, but requires a substantial number of simulated events in order to produce a clean parametrization in position, energy, zenith angle, and variables associated with shower multiplicities higher than one. The version of MuonGun at the time of writing provides the parametrizations for the Polygonato [91] and H4a [92] cosmic ray spectra. At the time of production for the analyses contained hereafter, all MuonGun simulation is produced assuming a multiplicity of 1, meaning that no bundles are yet produced with this generator. This is a limitation of simulation time: the multiplicity parametrizations vastly extend the parameter space and therefore require significantly more time and effort to handle correctly.

Noise-Only Events

While we only observe neutrinos and muons in the detector, we also observe a significant component of accidental triggers in the DeepCore array. These events, labeled *accidental triggers*, arise due to the low trigger threshold. In these events, no actual particle interactions due to muons or neutrinos are observed. Instead, detector noise alone satisfies the trigger conditions, producing an event.

Simulation of accidental triggers involves only the noise and electronics simulation. Because the events are relatively rare, the simulation requires a special mode, here called *long-frame* simulation, which produces continuous detector readout. Breaking the traditional concept of the "simulated event", these simulation sets instead produce a 100 ms long "event" of random detector noise. These hits are then run through the simulation of waveforms, coincidences, and triggering as a normal simulated event. After triggering, specialized code is used to divide the long-frame simulation into smaller events similar to neutrino and muon simulations as well as actual experimental readout.

Once the events are generated, weighting the events is relatively straightforward: the weight per event depends on the muon interaction rate and the total simulated time. The latter is straightforward to calculate, depending only on the number of long frame simulation events produced and the time window for each of these events. The former is important due to the definition of the accidental triggers. These events, by definition, may only occur when no muon or neutrino is interacting within the detector. The weight of the accidental triggers must account for this "deadtime" due to particle interactions. This rate, assumed to be approximately 2800 Hz, leads to a change in the effective livetime per event of roughly 15

Accidental triggers are computationally expensive to produce, given that they rely on a relatively rare property of random detector noise. In general, a few minutes of effective livetime can take up to two hours to create, with much of the processing time spent on DOMs and hits that do not make it into final triggered events. This limits the total effective livetime that can be simulated in realistic timescales. Current simulations used in this thesis total approximately two months of effective livetime.

4.1.2 Signal Generation

GENIE

Background simulation is only part of the generation in IceCube. Studies searching for neutrino candidate events require simulated signal events to infer properties of the original events. At energies ranging from approximately 1 GeV to 1 TeV, IceCube has adopted the *GENIE* event generator [94]. This code, used widely throughout the oscillation community, includes information about the various interactions, cross sections, and uncertainties involved in neutrino physics from reactor energies upward.

Events in the GENIE generator are produced first by selecting events from a pure power law with a given spectral index, often chosen to be either E^{-1} or E^{-2} depending on the purpose. These events are then forced to interact with an electron or nucleon within a specified volume in the ice assuming a constant target density.

The type of interaction is determined using the cross section for the given flavor and energy. The cross section model, an updated version of GRV98 [95], includes resonant, elastic, quasielastic, and deep inelastic events. Particles produced in the interaction are propagated out of the nucleus, with final state interactions included. Hadrons with energies less than 30 GeV produced in GENIE simulation are propagated individually to obtain the light output using GEANT4 [96, 97]. Above 30 GeV, the lower event-to-event variability permits the use of parametrized light output for hadrons.

The GENIE code includes tools to reweight events based on uncertainties in eg. the axial masses, cross sections, and various aspects of the interactions themselves [94]. These features are used to model uncertainties in the tau neutrino analysis presented in this thesis.

The code is regularly updated, including both new features and retuning of parametrizations to match the latest data. The events produced in this work use GENIE version 2.8.6.

Neutrino-Generator

At energies higher than approximately 100 GeV, there are two changes to the simulation code. At these energies, the contribution to the cross section from deep inelastic interactions becomes dominant while the other interactions become negligible, as expected from Figure 1.7 [20]. This allows the simplification of the cross section calculations with no loss

in generality. In addition, the cross section continues to rise linearly with the energy. This latter feature requires a detailed simulation of potential interactions far from the detector: namely, high energy neutrinos have a non-negligible chance of interacting while propagating through the Earth.

The *Neutrino-Generator* code (hereafter, *NuGen*) is designed to handle these higher energy interactions [98]. In this model, neutrinos are no longer produced and forced to interact in the ice directly. Instead, a neutrino is produced from a power law spectrum in the atmosphere surrounding the Earth. The event is then propagated through the planet, using the PREM model of the density layers in the Earth [47] to simulate potential interactions en route. Neutrinos which interact may be lost or may be regenerated following the decay of the daughter particles. Neutrinos arriving at the detector are then forced to interact in the detector fiducial volume, yielding a simulated event. Hadronic output is returned in the form of parametrized light output due to the large number of particles.

NuGen can be configured with various Earth models as well as different generation properties. For the studies contained herein, the *NuGen* files are produced with an E^{-2} spectrum and interact following the CSMS cross section.

4.2 Propagation of the Particles and Light

After generation, IceCube simulated events require two types of *propagation*. The first, the propagation of charged leptons, produces the energy losses in the detector due to continuous and stochastic emissions. These energy losses are then used to produce photons that may be propagated through the detector using models of the Antarctic glacier.

4.2.1 Lepton Propagation with PROPOSAL

The propagation of leptons in IceCube is performed using *PROPOSAL*, a software module which contains tools to simulate the propagation of leptons and hadrons with ionization, electron pair-production, bremsstrahlung, photonuclear interactions, and decay processes [99]. The Cherenkov light output from daughter particles in each case is handled by a parametrization of the associated energy deposition for a given true particle energy as shown in Figure 4.1.

PROPOSAL propagates the charged particles through the detector, producing a series of energy emissions associated with each propagated particle. The output of the *PROPOSAL* module is this series of energy emissions and the associated number of Cherenkov photons for each emission.

4.2.2 CLSim for Photon Propagation

Once the energy deposition at each position is calculated, the resulting photons must be propagated. There exist two modules which can handle this: Photon Propagation Code *PPC* and OpenCL Simulation Code *CLSim*. The differences are largely of implementation details and both have been verified to give identical results. Only the latter, *CLSim*, will be discussed here.

CLSim is a code designed to propagate emitted photons using ray tracing algorithms [100]. The independence of the individual photons is leveraged to perform the propagation of all photons in parallelized calculations using the OpenCL programming language [101]. Photons are then propagated through the ice with the current best-fit knowledge about the scattering and absorption properties, continuing until either absorbed or until they reach a DOM. Photons which reach DOMs are stored.

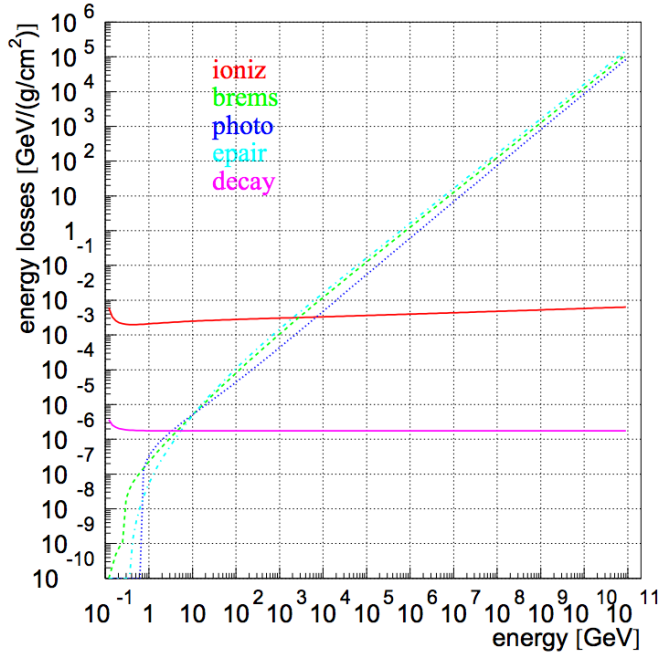


Figure 4.1 – Average energy losses ($\frac{-dE}{dx}$) for a muon in ice. At very low energies, ionization losses dominate. Above approximately 1 TeV, pair production and photonuclear effects become more important. Image taken from [21]

The propagation of individual photons is efficient at low energies, where the scattering of individual photons is important. At energies above a few hundred GeV, the light yield is large enough that the propagation of individual photons is both excessively costly as well as unnecessary. In those cases, a feature known as *oversizing* is used by setting a *oversize factor*, N_{OS} . The oversize factor, often set to 5 for IceCube simulations above 1 TeV, allows for the production of "weighted photons" representing photon bundles with size proportional to N_{OS}^2 , significantly reducing the computational power necessary for large numbers of photons. In order to compensate for the bundling of photons, the effective radius of the DOM is also increased by N_{OS} .

Oversizing is efficient for the simulation of high energy events with large numbers of photon. This breaks down at GeV energies, where the photon flux from an event is low and scattering or absorption of individual photons matters. Because of the complications associated with oversizing at low energies, most simulations of DeepCore events are done with the oversizing features disabled.

4.2.3 Angular Acceptance and Hole Ice

When photons reach the surface of a DOM, the *angular acceptance* is applied in order to model the hole ice. This acceptance, calculated from a combination of lab and in-situ measurements, represents the PMT efficiency as a function of the photon arrival direction. The acceptance has a negligible efficiency for photons arriving from the back of the PMT and high efficiency for photons reaching the face of the PMT as shown in Figure ???. All other directions follow a curve between these two points. The angular acceptance model used in this thesis uses an empirical form fit to flasher data with two free parameters, as shown in Figure 4.2. The most forward direction in the PMT, shown with $\cos(\eta) = 1$, is most affected by the bubble column (see Section 3.3.1).

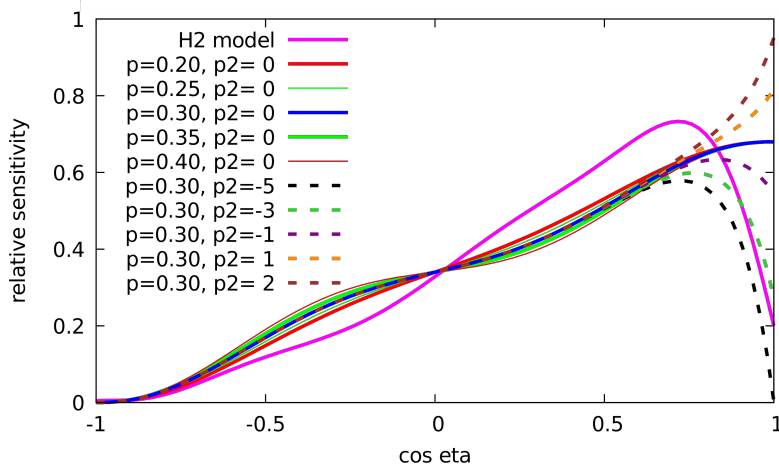


Figure 4.2 – Examples of the angular acceptance models used by IceCube. The relative sensitivity as a function of arrival direction is shown with $\cos(\eta) = -1$ indicating the back of the PMT and $\cos(\eta) = 1$ the face. The variation of the acceptance model used for this search is shown using by varying two parameters in the model. The ‘p’ parameter primarily controls the acceptance at the side of the DOM while the ‘p2’ parameter controls the acceptance from the forward region. A second model, H2, is also shown.

4.3 Simulating the Detector Electronics

4.3.1 Noise within IceCube-DeepCore

The noise simulation module used in IceCube, known as *Vuvuzela*, models the Poissonian and non-Poissonian detector noise using a set of five parameters, each representing distinct processes [71, 37].

The *thermal noise* and *radioactive decays* are Poisson processes simulated using rates fit during calibration. The thermal rate is correlated with the temperature and forms a large component of the noise in IceCube DOMs, with a typical rate of 200 Hz while the decay rate has a typical value of 50-100 Hz due to radioactive activity in the DOM glass. In order to model this bursting behavior described in Section 3.1.4, an effective model used which represents the timing of consecutive hits using a log-normal distribution. This introduces three additional parameters to the noise model: the average number of hits in a “burst”, giving the normalization; the mean time between hits within a burst; and the standard deviation of the timing within a burst. The non-Poissonian component to the noise model produces an additional 400 Hz of noise [71]. Noise hits in simulation are added as additional charge on each DOM at the face of the PMT.

The Vuvuzela model has previously been fit to each DOM in the detector, although with some limitations. Work completed during this thesis, discussed in Chapter 4.3.2, improved the calibration of the noise model.

4.3.2 PMTResponseSimulator and DOMLauncher

The IceCube detector does not directly measure photoelectrons emitted from the photocathode. Instead, IceCube events record the voltage response from the PMT via the output waveform. The production of simulated waveforms from incident photons is produced by a pair of modules.

The first module, *PMTResponseSimulator*, simulates the amplification process of the PMT, including the effects of pre-, late-, and afterpulsing. Each of these three effects

is modeled using calibration measurements performed in the lab. The second module, *DOMLauncher*, handles the local coincidence circuits, timing jitter of the DOM, the discriminator, and digitization simulation.

Bibliography

- [1] H. Becquerel. “Sur les radiations émises par phosphorescence”. In: *Comptes Rendus* 122 (1896) (cit. on p. 9).
- [2] J Chadwick. “Intensitätsverteilung im magnetischen Spectrum der β -Strahlen von radium B + C”. In: *Verhandl. Dtsc. Phys. Ges.* 16 (1914), p. 383 (cit. on p. 9).
- [3] W. Pauli. *Offener Brief an die Gruppe der Radioaktiven bei der Gauvereins-Tagung zu Tübingen*. ETH Zürich, 1930 (cit. on p. 9).
- [4] C. L. Cowan Jr., F. Reines, F. B. Harrison, H. W. Kruse, and A. D. McGuire. “Detection of the Free Neutrino: A Confirmation”. In: *Science* 124 (July 1956), pp. 103–104 (cit. on p. 9).
- [5] Nobel Foundation. *Nobel Prize in Physics*. 1995 (cit. on p. 10).
- [6] G. Danby, J-M. Gaillard, K. Goulian, et al. “Observation of High-Energy Neutrino Reactions and the Existence of Two Kinds of Neutrinos”. In: *Phys. Rev. Lett.* 9 (1 1962), pp. 36–44 (cit. on p. 10).
- [7] DONUT Collaboration, K. Kodama, N. Ushida, et al. “Observation of tau neutrino interactions”. In: *Physics Letters B* 504 (Apr. 2001), pp. 218–224. eprint: [hep-ex/0012035](#) (cit. on pp. 10, 18, 32).
- [8] K. Kodama, N. Ushida, C. Andreopoulos, et al. “Final tau-neutrino results from the DONuT experiment”. In: *Phys. Rev. D* 78.5, 052002 (Sept. 2008), p. 052002. arXiv: [0711.0728 \[hep-ex\]](#) (cit. on p. 10).
- [9] The ALEPH Collaboration, the DELPHI Collaboration, the L3 Collaboration, et al. “Precision Electroweak Measurements on the Z Resonance”. In: *ArXiv High Energy Physics - Experiment e-prints* (Sept. 2005). eprint: [hep-ex/0509008](#) (cit. on pp. 10, 26).
- [10] A. De Angelis. “Domenico Pacini, uncredited pioneer of the discovery of cosmic rays”. In: *ArXiv e-prints* (Mar. 2011). arXiv: [1103.4392](#) (cit. on p. 11).
- [11] J. R. Hoerandel. “Early cosmic-ray work published in German”. In: *American Institute of Physics Conference Series*. Ed. by J. F. Ormes. Vol. 1516. American Institute of Physics Conference Series. Feb. 2013, pp. 52–60. arXiv: [1212.0706](#) (cit. on p. 11).
- [12] Arthur H. Compton. “A Geographic Study of Cosmic Rays”. In: *Phys. Rev.* 43 (6 1933), pp. 387–403 (cit. on p. 11).
- [13] Nobel Foundation. *Nobel Prize in Physics*. 1936 (cit. on p. 11).
- [14] M Blau and H Wambacher. “Disintegration Processes by Cosmic Rays with the Simultaneous Emission of Several Heavy Particles”. In: 140 (Jan. 1937), pp. 585–585 (cit. on p. 11).

- [15] W. Bothe and W. Kolhoerster. “Das Wesen der Hoehenstrahlung”. In: *Zeitschrift fur Physik* 56 (Nov. 1929), pp. 751–777 (cit. on p. 11).
- [16] G. W. Clark, J. Earl, W. L. Kraushaar, et al. “Cosmic-Ray Air Showers at Sea Level”. In: *Phys. Rev.* 122 (2 1961), pp. 637–654 (cit. on p. 11).
- [17] K. A. Olive et al. “Review of Particle Physics”. In: *Chin. Phys. C*38 (2014), p. 090001 (cit. on pp. 11, 12, 17, 18, 22).
- [18] M. Honda, M. S. Athar, T. Kajita, K. Kasahara, and S. Midorikawa. “Atmospheric neutrino flux calculation using the NRLMSISE-00 atmospheric model”. In: *Phys. Rev. D* 92.2, 023004 (July 2015), p. 023004. arXiv: 1502.03916 [astro-ph.HE] (cit. on pp. 11, 13).
- [19] Wikimedia Commons. *File:Standard Model of Elementary Particles.svg* — *Wikimedia Commons, the free media repository*. [Online; accessed 23-February-2018]. 2017 (cit. on p. 14).
- [20] J. A. Formaggio and G. P. Zeller. “From eV to EeV: Neutrino cross sections across energy scales”. In: *Reviews of Modern Physics* 84 (July 2012), pp. 1307–1341. arXiv: 1305.7513 [hep-ex] (cit. on pp. 15, 16, 45).
- [21] D. Chirkin and W. Rhode. “Propagating leptons through matter with Muon Monte Carlo (MMC)”. In: *ArXiv High Energy Physics - Phenomenology e-prints* (July 2004). eprint: hep-ph/0407075 (cit. on pp. 17, 47).
- [22] H. Pessard. “The Opera Experiment”. In: *High Energy Physics, ICHEP 2004*. Ed. by H. Chen, D. Du, W. Li, and C. Lu. Apr. 2005, pp. 299–303. eprint: hep-ex/0504033 (cit. on pp. 18, 32).
- [23] Minos Collaboration, D. G. Michael, P. Adamson, et al. “The magnetized steel and scintillator calorimeters of the MINOS experiment”. In: *Nuclear Instruments and Methods in Physics Research A* 596 (Nov. 2008), pp. 190–228. arXiv: 0805.3170 [physics.ins-det] (cit. on p. 18).
- [24] S. Mufson, B. Baugh, C. Bower, et al. “Liquid scintillator production for the NOvA experiment”. In: *Nuclear Instruments and Methods in Physics Research A* 799 (Nov. 2015), pp. 1–9. arXiv: 1504.04035 [physics.ins-det] (cit. on p. 18).
- [25] L. Aliaga and et al. “Design, calibration, and performance of the MINERvA detector”. In: *Nuclear Instruments and Methods in Physics Research A* 743 (Apr. 2014), pp. 130–159. arXiv: 1305.5199 [physics.ins-det] (cit. on p. 18).
- [26] Y. Kudenko and T2K Collaboration. “The near neutrino detector for the T2K experiment”. In: *Nuclear Instruments and Methods in Physics Research A* 598 (Jan. 2009), pp. 289–295. arXiv: 0805.0411 [physics.ins-det] (cit. on p. 18).
- [27] M. Antonello, B. Baibussinov, V. Bellini, et al. “ICARUS at FNAL”. In: *ArXiv e-prints* (Dec. 2013). arXiv: 1312.7252 [physics.ins-det] (cit. on p. 18).
- [28] P. A. Čerenkov. “Visible Radiation Produced by Electrons Moving in a Medium with Velocities Exceeding that of Light”. In: *Physical Review* 52 (Aug. 1937), pp. 378–379 (cit. on p. 18).
- [29] P. A. Cherenkov. “Visible luminescence of pure liquids under the influence of - radiation”. In: *Dokl. Akad. Nauk SSSR* 2.8 (1934). [Usp. Fiz. Nauk93,no.2,385(1967)], pp. 451–454 (cit. on p. 18).

- [30] I. M. Frank and I. E. Tamm. “Coherent visible radiation of fast electrons passing through matter”. In: *Compt. Rend. Acad. Sci. URSS* 14.3 (1937). [Usp. Fiz. Nauk93,no.2,388(1967)], pp. 109–114 (cit. on pp. 18, 19).
- [31] D.J. Griffiths. *Introduction to Electrodynamics*. Ed. by Pearson Education Limited. Fourth. 2013 (cit. on p. 18).
- [32] S. Tavernier. *Experimental Techniques in Nuclear and Particle Physics*. Ed. by Springer-Verlag. 2010 (cit. on p. 19).
- [33] K.A. Olive and Particle Data Group. “Review of Particle Physics”. In: *Chinese Physics C* 38.9 (2014), p. 090001 (cit. on p. 19).
- [34] B. Aharmim, S. N. Ahmed, A. E. Anthony, et al. “Combined analysis of all three phases of solar neutrino data from the Sudbury Neutrino Observatory”. In: *Phys. Rev. C* 88.2, 025501 (Aug. 2013), p. 025501. arXiv: 1109.0763 [nucl-ex] (cit. on pp. 19, 24).
- [35] C. W. Walter. “The Super-Kamiokande Experiment”. In: *Neutrino Oscillations: Present Status and Future Plans*. Ed. by J. A. Thomas and P. L. Vahle. World Scientific Publishing Co, 2008, pp. 19–43 (cit. on p. 19).
- [36] F. Montanet. “Design and expected performance of the ANTARES neutrino telescope”. In: *Nuclear Physics B Proceedings Supplements* 87 (June 2000), pp. 436–438. eprint: astro-ph/0001380 (cit. on p. 19).
- [37] M. G. Aartsen, M. Ackermann, J. Adams, et al. “The IceCube Neutrino Observatory: instrumentation and online systems”. In: *Journal of Instrumentation* 12 (Mar. 2017), P03012. arXiv: 1612.05093 [astro-ph.IM] (cit. on pp. 19, 32, 34–37, 40, 48).
- [38] B. Pontecorvo. “Neutrino Experiments and the Problem of Conservation of Leptonic Charge”. In: *Sov. Phys. JETP* 26 (1968). [Zh. Eksp. Teor. Fiz.53,1717(1967)], pp. 984–988 (cit. on p. 20).
- [39] Z. Maki, M. Nakagawa, and S. Sakata. “Remarks on the Unified Model of Elementary Particles”. In: *Progress of Theoretical Physics* 28 (Nov. 1962), pp. 870–880 (cit. on p. 20).
- [40] C. Giganti, S. Lavignac, and M. Zito. “Neutrino oscillations: The rise of the PMNS paradigm”. In: *Progress in Particle and Nuclear Physics* 98 (Jan. 2018), pp. 1–54. arXiv: 1710.00715 [hep-ex] (cit. on pp. 21, 23, 26).
- [41] S. T. Petcov. “The Nature of Massive Neutrinos”. In: *Adv. High Energy Phys.* 2013 (2013), p. 852987. arXiv: 1303.5819 [hep-ph] (cit. on p. 21).
- [42] E. K. Akhmedov and A. Y. Smirnov. “Paradoxes of neutrino oscillations”. In: *Physics of Atomic Nuclei* 72 (Aug. 2009), pp. 1363–1381. arXiv: 0905.1903 [hep-ph] (cit. on p. 21).
- [43] A. Y. Smirnov. “The MSW Effect and Matter Effects in Neutrino Oscillations”. In: *Physica Scripta Volume T* 121 (Jan. 2005), pp. 57–64. eprint: hep-ph/0412391 (cit. on p. 23).
- [44] S. M. Bilenky. “Neutrino oscillations: brief history and present status”. In: *ArXiv e-prints* (Aug. 2014). arXiv: 1408.2864 [hep-ph] (cit. on p. 23).
- [45] V. Barger, K. Whisnant, S. Pakvasa, and R. J. N. Phillips. “Matter effects on three-neutrino oscillations”. In: *Phys. Rev. D* 22 (11 1980), pp. 2718–2726 (cit. on p. 23).

- [46] Super-Kamiokande Collaboration. *Prob3++*. 2012 (cit. on p. 23).
- [47] Adam M. Dziewonski and Don L. Anderson. “Preliminary reference Earth model”. In: *Physics of the Earth and Planetary Interiors* 25.4 (1981), pp. 297 –356 (cit. on pp. 23, 46).
- [48] John N. Bahcall. “Solar Neutrinos. I. Theoretical”. In: *Phys. Rev. Lett.* 12 (11 1964), pp. 300–302 (cit. on p. 23).
- [49] Raymond Davis. “Solar Neutrinos. II. Experimental”. In: *Phys. Rev. Lett.* 12 (11 1964), pp. 303–305 (cit. on p. 23).
- [50] Bruce T. Cleveland, Timothy Daily, Jr. Raymond Davis, et al. “Measurement of the Solar Electron Neutrino Flux with the Homestake Chlorine Detector”. In: *The Astrophysical Journal* 496.1 (1998), p. 505 (cit. on p. 23).
- [51] J. N. Abdurashitov, V. N. Gavrin, V. V. Gorbachev, et al. “Measurement of the solar neutrino capture rate with gallium metal. III. Results for the 2002-2007 data-taking period”. In: *Phys. Rev. C* 80.1, 015807 (July 2009), p. 015807. arXiv: 0901.2200 [nucl-ex] (cit. on p. 24).
- [52] W. Hampel, J. Handt, G. Heusser, et al. “GALLEX solar neutrino observations: results for GALLEX IV”. In: *Physics Letters B* 447.1 (1999), pp. 127 –133 (cit. on p. 24).
- [53] M. Altmann, M. Balata, P. Belli, et al. “Complete results for five years of GNO solar neutrino observations”. In: *Physics Letters B* 616.3 (2005), pp. 174 –190 (cit. on p. 24).
- [54] Herbert H. Chen. “Direct Approach to Resolve the Solar-Neutrino Problem”. In: *Phys. Rev. Lett.* 55 (14 1985), pp. 1534–1536 (cit. on p. 24).
- [55] Nobel Foundation. *Nobel Prize in Physics*. 2015 (cit. on pp. 24, 25).
- [56] Y. Fukuda, T. Hayakawa, E. Ichihara, et al. “Evidence for Oscillation of Atmospheric Neutrinos”. In: *Phys. Rev. Lett.* 81 (8 1998), pp. 1562–1567 (cit. on p. 25).
- [57] J. Bergström, M. C. Gonzalez-Garcia, M. Maltoni, and T. Schwetz. “Bayesian global analysis of neutrino oscillation data”. In: *Journal of High Energy Physics* 9, 200 (Sept. 2015), p. 200. arXiv: 1507.04366 [hep-ph] (cit. on p. 25).
- [58] I. Esteban, M. C. Gonzalez-Garcia, M. Maltoni, I. Martinez-Soler, and T. Schwetz (cit. on pp. 25, 26).
- [59] S. Gariazzo, C. Giunti, M. Laveder, Y. F. Li, and E. M. Zavanin. “Light sterile neutrinos”. In: *Journal of Physics G Nuclear Physics* 43.3, 033001 (Mar. 2015), p. 033001. arXiv: 1507.08204 [hep-ph] (cit. on pp. 26, 27).
- [60] J. M. Conrad, C. M. Ignarra, G. Karagiorgi, M. H. Shaevitz, and J. Spitz. “Sterile Neutrino Fits to Short Baseline Neutrino Oscillation Measurements”. In: *ArXiv e-prints* (July 2012). arXiv: 1207.4765 [hep-ex] (cit. on p. 26).
- [61] S. Gariazzo, C. Giunti, M. Laveder, and Y. F. Li. “Updated global 3+1 analysis of short-baseline neutrino oscillations”. In: *Journal of High Energy Physics* 6, 135 (June 2017), p. 135. arXiv: 1703.00860 [hep-ph] (cit. on pp. 26, 27).
- [62] P. Adamson, D. J. Auty, D. S. Ayres, et al. “Active to Sterile Neutrino Mixing Limits from Neutral-Current Interactions in MINOS”. In: *Physical Review Letters* 107.1, 011802 (July 2011), p. 011802. arXiv: 1104.3922 [hep-ex] (cit. on p. 27).

- [63] P. Adamson, I. Anghel, A. Aurisano, et al. “Search for Sterile Neutrinos Mixing with Muon Neutrinos in MINOS”. In: *Physical Review Letters* 117.15, 151803 (Oct. 2016), p. 151803. arXiv: 1607.01176 [hep-ex] (cit. on p. 27).
- [64] P. Adamson, L. Aliaga, D. Ambrose, et al. “Search for active-sterile neutrino mixing using neutral-current interactions in NOvA”. In: *Phys. Rev. D* 96.7, 072006 (Oct. 2017), p. 072006. arXiv: 1706.04592 [hep-ex] (cit. on p. 27).
- [65] K. Abe, Y. Haga, Y. Hayato, et al. “Limits on sterile neutrino mixing using atmospheric neutrinos in Super-Kamiokande”. In: *Phys. Rev. D* 91 (5 2015), p. 052019 (cit. on p. 27).
- [66] IceCube Collaboration, M. G. Aartsen, M. Ackermann, et al. “Search for sterile neutrino mixing using three years of IceCube DeepCore data”. In: *ArXiv e-prints* (Feb. 2017). arXiv: 1702.05160 [hep-ex] (cit. on p. 27).
- [67] M. G. Aartsen, K. Abraham, M. Ackermann, et al. “Searches for Sterile Neutrinos with the IceCube Detector”. In: *Physical Review Letters* 117.7, 071801 (Aug. 2016), p. 071801. arXiv: 1605.01990 [hep-ex] (cit. on pp. 27, 37).
- [68] Stephen Parke and Mark Ross-Lonergan. “Unitarity and the three flavor neutrino mixing matrix”. In: *Phys. Rev. D* 93 (11 2016), p. 113009 (cit. on pp. 28–30).
- [69] M. G. Aartsen, M. Ackermann, J. Adams, et al. “Calibration and characterization of the IceCube photomultiplier tube”. In: *Nuclear Instruments and Methods in Physics Research Section A: Accelerators, Spectrometers, Detectors and Associated Equipment* 618.1 (2010), pp. 139–152 (cit. on pp. 32, 33, 36).
- [70] Hammamatsu Photonics. *PHOTOMULTIPLIER TUBE DATA SHEET R7081-02 for ICECUBE Experiment*. 2003 (cit. on p. 32).
- [71] M. J. Larson. “Simulation and identification of non-Poissonian noise triggers in the IceCube neutrino detector”. M.Sc. Alabama U., 2013 (cit. on pp. 34, 35, 48).
- [72] R. Abbasi, Y. Abdou, T. Abu-Zayyad, et al. “The design and performance of IceCube DeepCore”. In: *Astroparticle Physics* 35 (May 2012), pp. 615–624. arXiv: 1109.6096 [astro-ph.IM] (cit. on pp. 36, 37).
- [73] M. G. Aartsen, R. Abbasi, Y. Abdou, et al. “Measurement of South Pole ice transparency with the IceCube LED calibration system”. In: *Nuclear Instruments and Methods in Physics Research A* 711 (May 2013), pp. 73–89. arXiv: 1301.5361 [astro-ph.IM] (cit. on pp. 36, 39, 40).
- [74] The HAWC Collaboration and The IceCube Collaboration. “Combined Analysis of Cosmic-Ray Anisotropy with IceCube and HAWC”. In: *ArXiv e-prints* (Aug. 2017). arXiv: 1708.03005 [astro-ph.HE] (cit. on p. 37).
- [75] M. G. Aartsen, G. C. Hill, A. Kyriacou, et al. “Measurement of the multi-TeV neutrino interaction cross-section with IceCube using Earth absorption”. In: *Nature* 551 (Nov. 2017), pp. 596–600. arXiv: 1711.08119 [hep-ex] (cit. on p. 37).
- [76] M. G. Aartsen, K. Abraham, M. Ackermann, et al. “Observation and Characterization of a Cosmic Muon Neutrino Flux from the Northern Hemisphere Using Six Years of IceCube Data”. In: *Ap.J.* 833, 3 (Dec. 2016), p. 3. arXiv: 1607.08006 [astro-ph.HE] (cit. on p. 37).
- [77] IceCube Collaboration. “Evidence for High-Energy Extraterrestrial Neutrinos at the IceCube Detector”. In: *Science* 342, 1242856 (Nov. 2013), p. 1242856. arXiv: 1311.5238 [astro-ph.HE] (cit. on p. 38).

- [78] S. Euler. “Observations of Oscillations of Atmospheric Neutrinos with the IceCube Neutrino Observatory”. Ph.D. Rheinisch-Westfälische Technische Hochschule (RWTH), 2013 (cit. on pp. 38, 39).
- [79] M. G. Aartsen, R. Abbasi, Y. Abdou, et al. “Measurement of Atmospheric Neutrino Oscillations with IceCube”. In: *Physical Review Letters* 111.8, 081801 (Aug. 2013), p. 081801. arXiv: 1305.3909 [hep-ex] (cit. on p. 37).
- [80] IceCube Collaboration, M. G. Aartsen, M. Ackermann, et al. “Determining neutrino oscillation parameters from atmospheric muon neutrino disappearance with three years of IceCube DeepCore data”. In: *ArXiv e-prints* (Oct. 2014). arXiv: 1410.7227 [hep-ex] (cit. on p. 37).
- [81] IceCube Collaboration, M. G. Aartsen, M. Ackermann, et al. “Measurement of Atmospheric Neutrino Oscillations at 6–56 GeV with IceCube DeepCore”. In: *ArXiv e-prints* (July 2017). arXiv: 1707.07081 [hep-ex] (cit. on p. 37).
- [82] M. G. Aartsen, M. Ackermann, J. Adams, et al. “Search for annihilating dark matter in the Sun with 3 years of IceCube data”. In: *European Physical Journal C* 77, 146 (Mar. 2017), p. 146. arXiv: 1612.05949 [astro-ph.HE] (cit. on p. 39).
- [83] M. G. Aartsen, K. Abraham, M. Ackermann, et al. “All-flavour search for neutrinos from dark matter annihilations in the Milky Way with IceCube/DeepCore”. In: *European Physical Journal C* 76, 531 (Oct. 2016), p. 531. arXiv: 1606.00209 [astro-ph.HE] (cit. on p. 39).
- [84] N. E. Bramall, R. C. Bay, K. Woschnagg, R. A. Rohde, and P. B. Price. “A deep high-resolution optical log of dust, ash, and stratigraphy in South Pole glacial ice”. In: *Geophys. Res. Lett.* 32, L21815 (Nov. 2005), p. L21815 (cit. on p. 39).
- [85] M. Ackermann, J. Ahrens, X. Bai, et al. “Optical properties of deep glacial ice at the South Pole”. In: *Journal of Geophysical Research (Atmospheres)* 111, D13203 (July 2006), p. D13203 (cit. on p. 39).
- [86] IceCube Collaboration. *IceCube Dust Map*. 2011. URL: <http://icecube.berkeley.edu/~bay/dustmap/> (cit. on p. 39).
- [87] IceCube Collaboration, M. G. Aartsen, R. Abbasi, et al. “The IceCube Neutrino Observatory Part VI: Ice Properties, Reconstruction and Future Developments”. In: *ArXiv e-prints* (Sept. 2013). arXiv: 1309.7010 [astro-ph.HE] (cit. on p. 40).
- [88] M. Rongen. “Measuring the optical properties of IceCube drill holes”. In: *European Physical Journal Web of Conferences*. Vol. 116. European Physical Journal Web of Conferences. Apr. 2016, p. 06011 (cit. on p. 40).
- [89] D. Heck, G. Schatz, T. Thouw, J. Knapp, and J. N. Capdevielle. “CORSIKA: A Monte Carlo code to simulate extensive air showers”. In: (1998) (cit. on p. 42).
- [90] E.-J. Ahn, R. Engel, T. K. Gaisser, P. Lipari, and T. Stanev. “Cosmic ray interaction event generator SIBYLL 2.1”. In: *Phys. Rev. D* 80.9, 094003 (Nov. 2009), p. 094003. arXiv: 0906.4113 [hep-ph] (cit. on p. 42).
- [91] Joerg R. Hoerandel. “On the knee in the energy spectrum of cosmic rays”. In: *Astropart. Phys.* 19 (2003), pp. 193–220. arXiv: astro-ph/0210453 [astro-ph] (cit. on pp. 42, 44).
- [92] T. K. Gaisser, T. Stanev, and S. Tilav. “Cosmic ray energy spectrum from measurements of air showers”. In: *Frontiers of Physics* 8 (Dec. 2013), pp. 748–758. arXiv: 1303.3565 [astro-ph.HE] (cit. on pp. 43, 44).

- [93] Jakob van Santen. “Neutrino Interactions in IceCube above 1 TeV: Constraints on Atmospheric Charmed-Meson Production and Investigation of the Astrophysical Neutrino Flux with 2 Years of IceCube Data taken 2010–2012”. PhD thesis. U. Wisconsin, Madison (main), 2014-11-18 (cit. on p. 43).
- [94] C. Andreopoulos, C. Barry, S. Dytman, et al. “The GENIE Neutrino Monte Carlo Generator: Physics and User Manual”. In: *ArXiv e-prints* (Oct. 2015). arXiv: 1510.05494 [hep-ph] (cit. on p. 45).
- [95] M. Gluck, E. Reya, and A. Vogt. “Dynamical parton distributions revisited”. In: *European Physical Journal C* 5 (Sept. 1998), pp. 461–470. eprint: hep-ph/9806404 (cit. on p. 45).
- [96] S. Agostinelli et al. “GEANT4: A Simulation toolkit”. In: *Nucl. Instrum. Meth.* A506 (2003), pp. 250–303 (cit. on p. 45).
- [97] Makoto Asai, Andrea Dotti, Marc Verderi, and Dennis H. Wright. “Recent developments in Geant4”. In: *Annals Nucl. Energy* 82 (2015), pp. 19–28 (cit. on p. 45).
- [98] A. Gazizov and M. Kowalski. “ANIS: High energy neutrino generator for neutrino telescopes”. In: *Computer Physics Communications* 172 (Nov. 2005), pp. 203–213. eprint: astro-ph/0406439 (cit. on p. 46).
- [99] J. H. Koehne, K. Frantzen, M. Schmitz, et al. “PROPOSAL: A tool for propagation of charged leptons”. In: *Comput. Phys. Commun.* 184 (2013), pp. 2070–2090 (cit. on p. 46).
- [100] Dmitry Chirkin. “Photon tracking with GPUs in IceCube”. In: *Nucl. Instrum. Meth.* A725 (2013), pp. 141–143 (cit. on p. 46).
- [101] John E. Stone, David Gohara, and Guochun Shi. “OpenCL: A Parallel Programming Standard for Heterogeneous Computing Systems”. In: *IEEE Des. Test* 12.3 (May 2010), pp. 66–73 (cit. on p. 46).

Notes

█	find good quality swedish camera pics?	40
█	multinest	69
█	martin's thesis	71
█	millipede paper	71
█	martin's thesis	71
█	list of atmo disappearance measurements that use zenith and energy binning	76
█	dragon, leesard 3 year papers	76
█	dragon, leesard	76
█	cumulative plot of track length	76
█	cumulative plot of deltalh	76
█	roc curves for track length	76
█	this sentence needs to be reworded. its too verbose	76
█	mc templates!	77
█	nufit 2.2	77
█	PDG	77
█	superk paper, opera paper sources for unoscillating NC	77
█	non-sterile explanations of non-unitarity? maybe the neutrino decay paper?	78
█	think up a better phrasing to introduce the tau normalization	78
█	Crazy shit that I will probably take out. but maybe find the neutrino decay paper again?	78
█	opera tau neutrino event views	78
█	opera paper: https://arxiv.org/abs/1507.01417	78
█	superk paper on appearance https://arxiv.org/pdf/1711.09436.pdf	79
█	https://arxiv.org/pdf/1711.09436.pdf again	79
█	wtf is going on here? table 1 in the paper gives an expectation of 185.2 events, but the stuff at the top right of page 11 says the expectation is 224...?! and NIETHER of these give the 1.47 that they quote. wtf	79
█	figure 14 of https://arxiv.org/pdf/1711.09436.pdf	79
█	nufit 2.2	79
█	genie	80
█	coin fraction figure	83
█	Hammamatsu quantum efficiency? http://www.hamamatsu.com/resources/pdf/etd/LARGE_AREA_PMT TPMH1286E.pdf	83
█	How many were tested in a lab before deployment?	83
█	Where does the domeff prior come from?	83
█	domeff	83
█	ice model	83
█	bulk ice uncertainties vs depth	83
█	absorption	84

[green]	scattering	84
[green]	hole ice and hifwd	84
[purple]	how do i flesh this out?	85
[green]	muongun rates vs domeff and absorption to justify exponentials	85
[purple]	Need to include some discussion of th goodness of fit for these sets. Maybe a plot of the chi2 values for all of the sets?	85
[green]	chi2 values for hyperplane parametrizations	85
[purple]	This needs work. can't even be called a derivation. its just crap.	85
[green]	make a plot showing chi2 value as a function of mc stats scale factor to justify the 10x rule	86
[purple]	this is only true for muons! how do i explain that?	86
[orange]	All of these references for the priors...	87
[purple]	Maybe all of this oscfit stuff should just be moved to just before the systematics section.	89
[purple]	should i even talk about oscfit itself? it seems a bit awkward	89
[orange]	msu and desy disappearance	89
[green]	Flowchart of oscfit fitting. at least broadly	89
[orange]	prob3++	89
[orange]	nufit 2.2	89
[orange]	iminuit	89
[orange]	asimov expectation?	90
[green]	asimov sensitivity	90
[green]	brazilian flag	91
[green]	comparison of stat-only fit to full systematics fit	94
[green]	N+1 tests	94
[green]	N-1 tests	95
[green]	hidden potential martin n-1 tests	95
[red]	should i be including the dropped dis/theta13 systematics here? and maybe deltacp? otherwise this section feels a bit pointless	95
[red]	may just remove the burn sample crap. its so out of date that its too weird to go back and redo it.	95
[purple]	blahdy blahdy blahdy. no point spending time here if i may just kill it	95
[orange]	scipy	96
[green]	q/nch at L7	96
[orange]	wavedeform?	96
[orange]	TA003 charge template	97
[green]	example of shifted and unshifted charges for eg numu	98
[orange]	scipy rectbivariate spline	98
[green]	2d splines for mc charge scale correction	98
[green]	systematic effect of mc charge scale	98
[green]	figure 4.2.3 from my wiki	98
[red]	find the best-fit of the mc charge scale	98
[red]	what was the change in the pvalue from the mc charge scale?	98
[orange]	internal search for flaring doms	99
[green]	charge rms with the excess in data	101
[red]	find the number removed by the charge rms cut in data	101
[red]	percent reduction in number of data events	101
[green]	reco z distribution showing disagreement with data	101
[green]	reco energy up to a tev showing the disagreement due to bedrock	101

█████	awkward line connecting the disagreement in recoz to high reco energy	101
███	reco z of overlapping events in nugen and genie showing the bedrock problems .	102
███	reference the reco z plot showing bedrock issues again	102
███	energy and z distributions after reweighting genie bedrock events	102
█████	these updates with event rates should be lines on a data/mc rate table in the selection section	102
███	PDFs for gof	102
███	future reference to martin, elim's theses	107
███	elim's thesis	107
███	iminuit	107
███	elim's result!	107
███	icecube 2017 result	107
███	superk 2015 oscillation result	107
███	minos oscillation with atm	107
███	nova oscillation	107
███	t2k oscillation result	107
███	nufit 3.2	107
███	martin's thesis	107
███	martin's kdes from the aachen group. who did that?	107
███	pingu paper and/or pisa paper describing nmo measurement	108
███	Need martin's final result!	108
███	chi2 scans of the detector systematics to show greco constraints on domeff, holeice, hifwd, absorption, and scattering	108
█████	change cc and nc+cc to exclusive and inclusive respectively?	108
███	superk result	108
███	opera result	108
███	what's the livetime increase from loosing the GRL?	109
███	check the run dates	109